

Article

Revisiting the Bøggild Intergrowth in Iridescent Labradorite Feldspars: Ordering, Kinetics, and Phase Equilibria

Shiyun Jin ^{1,2}, Huifang Xu ^{1,*}  and Seungyeol Lee ^{1,3,4} 

¹ Department of Geoscience, University of Wisconsin-Madison, 1215 W. Dayton Street, Madison, WI 53706, USA; sjin48@wisc.edu (S.J.); lee572@wisc.edu (S.L.)

² Gemological Institute of America, 5355 Armada Drive, Carlsbad, CA 92008, USA

³ USRA Lunar and Planetary Institute, 3600 Bay Area Boulevard, Houston, TX 77058, USA

⁴ Astromaterials Research and Exploration Directorate, NASA Johnson Space Center, 2101 NASA Parkway, Houston, TX 77058, USA

* Correspondence: hfxu@geology.wisc.edu; Tel.: +1-608-265-5887

Abstract: The enigmatic Bøggild intergrowth in iridescent labradorite crystals was revisited in light of recent work on the incommensurately modulated structures in the intermediated plagioclase. Five igneous samples and one metamorphic labradorite sample with various compositions and lamellar thicknesses were studied in this paper. The lamellar textures were characterized with conventional transmission electron microscopy (TEM) and scanning transmission electron microscopy (STEM). The compositions of individual lamellae were analyzed with high-resolution energy-dispersive X-ray spectroscopy (EDS) mapping and atom probe tomography (APT). The average structure states of the studied samples were also compared with single-crystal X-ray diffraction data (SC-XRD). The Na-rich lamellae have a composition of An_{44-48} , and the Ca-rich lamellae range from An_{56} to An_{63} . Significant differences between the lamellar compositions of different samples were observed. The compositions of the Bøggild intergrowth do not only depend on the bulk compositions, but also on the thermal history of the host rock. The implications on the subsolidus phase relationships of the plagioclase feldspar solid solution are discussed. The results cannot be explained by a regular symmetrical solvus such as the Bøggild gap, but they support an inclined two-phase region that closes at low temperature.

Keywords: labradorite; Bøggild intergrowth; *e*-plagioclase; incommensurately modulated structures; exsolution lamellae; phase diagram



check for updates

Citation: Jin, S.; Xu, H.; Lee, S. Revisiting the Bøggild Intergrowth in Iridescent Labradorite Feldspars: Ordering, Kinetics, and Phase Equilibria. *Minerals* **2021**, *11*, 727. <https://doi.org/10.3390/min11070727>

Academic Editor:
Emanuela Schingaro

Received: 22 June 2021
Accepted: 2 July 2021
Published: 5 July 2021

Publisher's Note: MDPI stays neutral with regard to jurisdictional claims in published maps and institutional affiliations.



Copyright: © 2021 by the authors. Licensee MDPI, Basel, Switzerland. This article is an open access article distributed under the terms and conditions of the Creative Commons Attribution (CC BY) license (<https://creativecommons.org/licenses/by/4.0/>).

1. Introduction

Labradorite feldspar is the intermediate to calcic member of the plagioclase feldspar series, the solid solution between albite (Ab: $NaAlSi_3O_8$) and anorthite (An: $CaAl_2Si_2O_8$). It is defined to be plagioclase feldspar with a composition between An_{50} (half albite and half anorthite) and An_{70} (70% anorthite and 30% albite). The name labradorite was originally from its type locality, Paul's Island in Labrador, Canada, where the labradorite crystals are characterized by the iridescent optical effect when reflecting light [1]. This interference color, variously known as the “labradorescence” or “schiller” effect [2], has attracted the interest of mineralogists and physicists for centuries. The earliest systematic study of labradorescence started around 100 years ago [3,4]. Ove Balthasar Bøggild [4] first measured the orientations of the reflection planes relative to the crystallographic planes in the labradorite crystals, and also coined the word labradorescence. The exsolution texture in labradorite that produces the labradorescence has therefore been named after him as the Bøggild intergrowth.

Previous works on the iridescent colors and lamellar textures have been nicely summarized by Ribbe [2], and Smith and Brown [5]. All labradorite feldspars showing labradorescence are found in igneous rocks with extremely slow cooling rates, with bulk compositions

ranging from $An_{46\pm 2}$ to and $An_{60\pm 2}$ [2]. The lamellar period, or the wavelength of the iridescent color, increases systematically with the $An\#$ of the bulk composition of the labradorite, along with the volume ratio between Ca-rich and Na-rich lamellae. All the Bøggild intergrowths ever observed have been at the submicron scale with a period ranging from ~150 to ~300 nm. This narrow range of scale of exsolution texture is unique, and it poses challenges in analyzing the composition of individual lamellae. Several attempts have been made on isolated labradorite samples, using the electron probe [6–8] and ion probe [9] as direct methods, or differences in Kikuchi patterns [10] or in the e -fringes (orientation and period of the modulation) [11] as indirect methods. The results, however, seemed to vary quite a bit from one sample to another, or between different methods, although most have suggested a compositional difference of ~10–15 mol% An between the Ca-rich (major) and Na-rich (minor) lamellae.

As a result of the slow cooling rate, all iridescent labradorite crystals are well ordered e -plagioclase, which is an incommensurately modulated phase of the plagioclase solid solution, appearing at low temperature with intermediate composition (between ~ An_{25} and ~ An_{75}). The e -plagioclase structures are characterized by satellite reflections (e -reflections) in the diffraction pattern that appears around the absent b -reflections. The e -plagioclase can be further divided into two different phases, $e1$ and $e2$, which were previously separated by composition [5,12,13] and were later discerned by the presence or absence of the f -reflections (second-order satellites) in the diffraction pattern [14,15], respectively. The $e1$ structure displays a density modulation, which is the variation in composition along the modulated structures, whereas in the $e2$ structure, no compositional variation is present, and the modulation only results in a distorted framework and local ordering of cations [14,15]. Previous X-ray diffraction work in iridescent labradorite crystals has indicated the presence of a strong density modulation [15–23]; thus, at least one member (most likely both) of the Bøggild intergrowth is of the $e1$ structure.

The Bøggild intergrowth occurs in the middle of the plagioclase solid solution, where the subsolidus phase relation is most complicated. Four different phases may occur in this composition range, $C\bar{1}$, $I\bar{1}$, $e1$, and $e2$. Several phase diagrams have been proposed over the decades, some with completely different topologies around the Bøggild intergrowth [5,12,13,24–28]. One of the complications comes from complicated structures of the e -plagioclase phase, the thermodynamic stability of which was not officially recognized before the phase diagram proposed by Carpenter [13]. Recent studies on the crystal structures of intermediate plagioclase feldspars [14,15,23,29–32] have revealed a more systematic relation among the ordering state, composition, and cooling history in natural crystals. With these new understandings of the intermediate plagioclase, we revisited the Bøggild intergrowth by studying several iridescent labradorite samples from different locations, using a combination of conventional transmission electron microscopy (TEM), scanning transmission electron microscopy (STEM), atom probe tomography (APT), and single crystal X-ray diffraction (SCXRD) methods. Some details in exsolution texture, composition profile, and structure variations were revealed that were not known before. Their implications and some possible topologies of the phase relations around the Bøggild gap are discussed.

2. Materials and Methods

Five igneous labradorite samples plus one metamorphic plagioclase sample were studied in this work. Some optical images of the samples used in this paper can be found in Figures S1 and S2. All the igneous samples were from Proterozoic anorthosite rocks, showing iridescent color with zonation. Large crystals with color and compositional zoning were purposely selected for this study, for ease of comparison of the effect of bulk composition on the exsolution process with the same thermal history. All the igneous crystals are quite similar in appearance, with dark colors resulting from the iron oxide inclusions/precipitates in the crystals (Figure S2). Sample Gem118 shows the darkest color of all, with high-density needle-shaped opaque inclusions, and sample MAD shows the

lightest body color (yellow), with much fewer inclusions in the crystal. The inclusions in sample Gem113 are mostly flaky hematite with the same orientation, which produces a strong aventurescence effect (optical effect commonly observed in sunstones) with light shined at a certain angle. The exact mechanism responsible for the iron oxide inclusions in labradorite or other feldspar minerals is not well understood [5]. Sample VB shows the smallest crystals of all the igneous samples, and the color zoning is much more heterogeneous and fine-scaled, most likely as a result of a faster cooling rate compared to the other crystals. The metamorphic sample 987L was found in a metamorphosed carbonate rock near Augusta, Maine [33], and was first studied by Grove et al. [27] using TEM, which showed no exsolution lamellae. Jin and Xu [14] confirmed this TEM observation and refined its incommensurately modulated structure using single-crystal X-ray diffraction. Surprisingly, further investigation revealed that crystals with slightly more sodic compositions from the same rock chip show interesting exsolution textures, and they were, therefore, selected for this work for comparison with the igneous samples. A summary of the locality, composition ranges, and compositions of individual iridescent color zones is listed in Table 1. The chemical compositions of the samples were analyzed with a CAMECA SXFive field-emission electron probe micro-analyzer (EPMA). The results of the EPMA analyses can be found in Table S1.

Table 1. Names, provenances, composition ranges, and compositions of individual color zones of the samples studied in this paper.

Sample ¹	Locality ²	Or#	An# Range	Red ³	Yellow	Blue
Gem118	Finland	2.4–4.0	55–58	58	N/A	55
VB (Volga Blue)	Ukraine	2.0–2.8	52–61	N/A	55–56	54
Gem113	NL, Canada	2.2–3.0	52–54	54	N/A	52
R2923	Sweden	2.3–2.7	50–53	52.5	N/A	51
MAD	Madagascar	2.3–3.1	49–52	52	51	49
987L	ME, USA	0.5–0.9	48–52		49 ⁴	

¹ The crystal structures of sample VB, R2923, and 987L have been reported in recent papers [14,15,23]. ² Sample VB and Gem113 were from the UW-Madison mineral collection; sample R2923 was from the Smithsonian National Museum of Natural History; sample 987L was from Timothy L. Grove [27]; sample Gem118 and MAD were purchased from mineral shops. ³ The iridescent colors were roughly classified into red, yellow, and blue, even though the exact color can be different between different samples (Figure S1). ⁴ The crystals of sample 987L (metamorphic rock) were too small for any iridescent color to be observed. Evidence of the exsolution texture can only be found with TEM.

The TEM and STEM samples of the igneous labradorites were prepared by crushing small plagioclase grains selected from an area close to the points analyzed by EPMA in ethanol with an agate mortar. Drops of the suspension were placed on lacey-carbon-coated Cu grids, and the small flaky crystals were left on the Cu grid after the ethanol evaporated. Ion-milling was not used for these larger crystals, to best avoid surface contamination and damage. Ion-milled samples were used for sample 987L. A 3 mm copper ring was mounted onto a 30 µm-thick optical thin section by epoxy glue with the area of interest in the center, and it was then cut out from the thin section and soaked in acetone to eliminate the mounting adhesive on the sample. The sample was ion milled with a Fischione 1050 at 5.2 kV for about 8 h at a 10° angle, and it was then milled at 1.3 kV for another half hour to minimize the amorphous matter on the sample. The sample was coated with a thin layer of carbon before being examined with TEM. TEM images and selected-area electron diffraction patterns (SAED) were taken using a Philips CM200UT TEM. The STEM images and X-ray EDS maps were collected with an FEI Talos F200X TEM/STEM.

The complete X-ray diffraction data were collected on a Bruker Quazar APEXII single-crystal diffractometer with a MoK α I μ S source and APEX2 detector. Different scan widths and exposure times were planned for each dataset depending on the different intensities and separations of the satellite peaks in each sample. The instrument was run at 50 kV and 0.6 mA. Unit-cell parameters were calculated and refined using APEX3 software. The intensities of the reflections in the diffraction data were also integrated and corrected with

APEX3. Crystal structures were refined using the JANA2006 program [34]. The CIF file of the refined crystal structures can be found in Supplementary Materials.

The sample for atom probe tomography (Gem118) was carefully cut to a small slab perpendicular to the *a*-axis, which was thick enough for the iridescent color zoning to be observed on the side of the slab. The microtip specimens for atom probe analysis were prepared with an FEI Nova 200 Dual-Beam FIB-SEM, using standard lift-out, mounting, and sharpening techniques to produce the desired specimen shape. The prepared microtips were analyzed using a pulsed laser with the Cameca Local Electrode Atom Probe (LEAP) 4000× HR instrument at the Center for Nanophase Materials Sciences (CNMS) of Oak Ridge National Laboratory. The atom probe data were reconstructed and analyzed using the Integrated Visualization and Analysis System (IVAS).

3. Results

3.1. TEM and STEM

The TEM images (Figures S3–S9) of the iridescent labradorite samples mostly confirm the previous studies on the Bøggild intergrowth [2,5]. The red-iridescent area in all of the igneous samples shows lamellar periods of about 300–350 nm, with the Ca-rich lamellae (~200 nm) about twice as thick as the Na-rich lamellae (~100 nm). The blue-iridescent area, on the other hand, shows a lamellar period of around 160 nm, with Ca-rich and Na-rich lamellae about equal in thickness (~80 nm).

Higher-magnification images of the [311] zone axis, along with the corresponding electron diffraction patterns, are shown in Figure 1 for both the red-iridescent area (A_{N54}) and the blue-iridescent area (A_{N52}) of sample Gem113. The images show both the modulation *e*-fringes pattern and the exsolution lamellar feature. It is known that the modulation directions of *e*-plagioclase structures fall almost exactly onto the [923] zone axis, which is very close to the [311] axis (~9° off) [5]. Bøggild's measurements of the Canadian samples also showed lamellar orientations close to $(\bar{9} 33 4)$ [4]. The geometrical relations among the [311] axis, [923] axis, and $(\bar{9} 33 4)$ plane are shown in Figure 2, with the orientations of modulation directions for some compositions marked on the [923] zone axis. There is an obvious change in the modulation period and orientation across the exsolution lamellar boundary (Figure 1). The change is more dramatic in the blue-iridescent area (~18° blue vs. ~11° red), suggesting that the compositional difference between adjacent lamellae in the blue-iridescent area is larger than the difference in the red-iridescent area. The boundary is not a perfectly straight line, but a transition zone about 20 nm in width with a sawtooth shape. The *e*-fringes are straight within each individual lamella, suggesting a homogeneous composition within each lamella. It is worth noting that such a comparison between different iridescent-colored areas is only meaningful with the same zone-axis images, because *e*-fringes are projections of a three-dimensional modulated structure that would change with the orientation of the electron beam. The high-resolution image of the red-iridescent area, which shows the *e*-fringes across the lamellar boundary, seem to be much harder to acquire compared to the blue-iridescent area, perhaps resulting from a slight variation in the boundary orientation. This might explain why most of the previously published images of Bøggild intergrowths with clear *e*-fringes are from blue-iridescent samples with equal lamellar thicknesses [2,11,35,36]. The electron diffraction pattern of the blue-iridescent area shows obviously split *e*-reflections corresponding to the Ca-rich and Na-rich lamellae, respectively. The *e*-reflections from the Ca-rich lamellae are much stronger than those from the Na-rich lamellae, even though they are about equal in volume. The diffraction pattern of the red area shows asymmetrical pear-shaped *e*- and *f*-reflections with no obvious splitting. The elongation of the *f*-reflections suggests that both Ca-rich and Na-rich lamellae are *e*1 structures. A similar TEM image of the blue-iridescent area of sample MAD, along with the selected area fast Fourier transform (FFT) of the Ca-rich and Na-rich lamellae, is provided in Figure S6. The change in orientation of the *e*-fringes in sample MAD is slightly smaller (~12°). The FFT from both the Ca-rich and Na-rich lamellae show sharp and strong *f*-reflections.

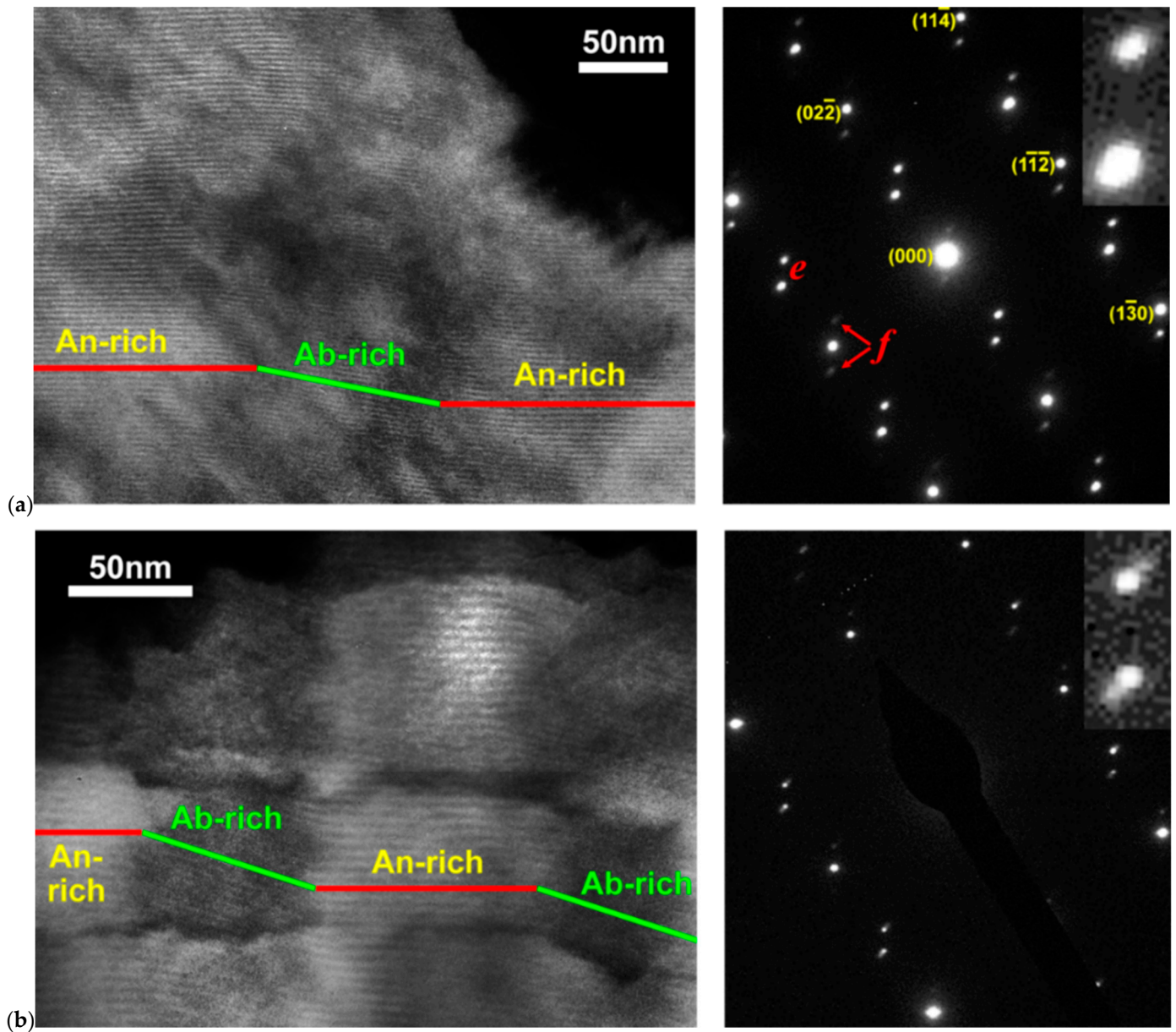


Figure 1. High-resolution dark-field TEM images of both red-iridescent (a) and blue-iridescent (b) areas in sample Gem113, showing both the exsolution lamellar boundaries and the modulation *e*-fringes. The corresponding selected-area diffraction patterns (SAED) of the [311] zone axis are shown to the right of the images. The blue-iridescent sample shows a much larger change in the modulation direction and period compared to the red-iridescent sample, which is also reflected in the SAED pattern.

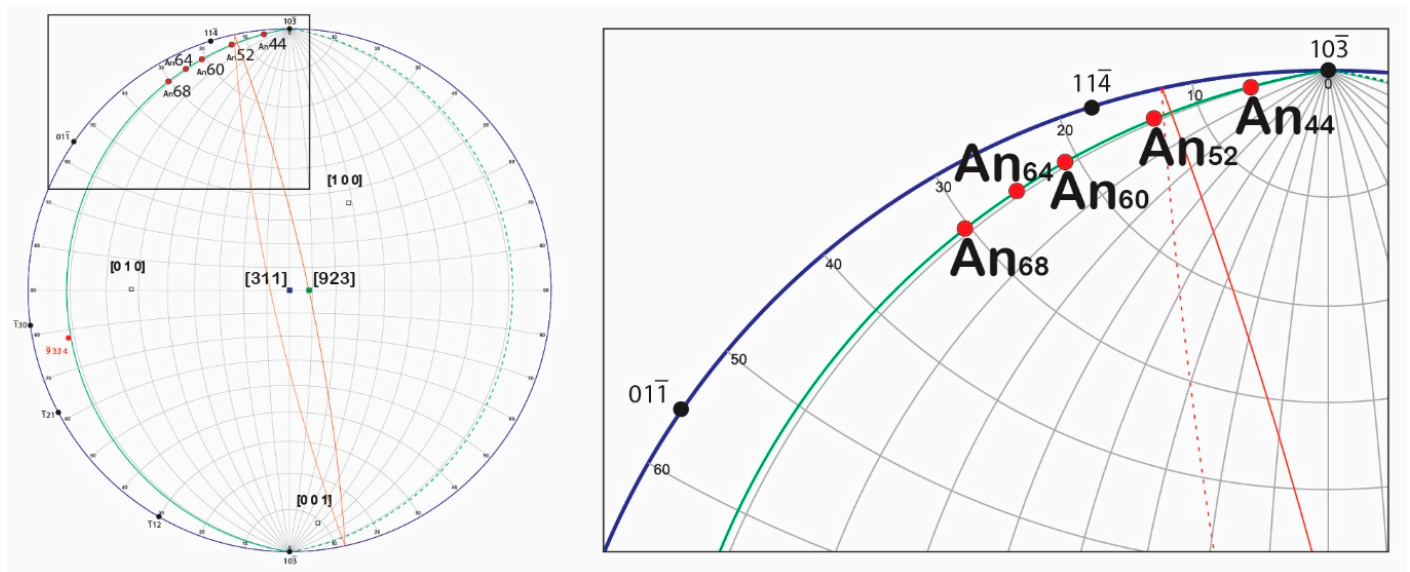


Figure 2. Stereonet projection of the modulation vectors along with the exsolution lamellar orientation, viewing along the $[311]$ axis. The modulation vectors are averaged from the data of the e_α structures in Jin et al. [23]. The modulation vector moves on the $[923]$ zone axis away from $(10\bar{3})$ about 1° for every 1 mol% more An in composition.

A high-angle annular dark-field (HAADF) STEM image of the ion milled sample 987L is shown in Figure 3. The signals collected by the HAADF detector directly correlate with the local mass-thickness; therefore, the contrast is directly correlated with chemical variations in the sample, with Ca-rich lamellae appearing bright and Na-rich lamellae dark in the image. The lamellae in sample 987L are not as periodic as the igneous samples and show a wide range of thicknesses within a small area. The combined width of adjacent Ca-rich and Na-rich lamellae ranges from more than 300 nm to less than 130 nm. The Na-rich lamellae in sample 987L appears much thinner than any igneous labradorite studied, resulting in the highest volume ratio between the Ca-rich and Na-rich lamellae. Energy-dispersive X-ray spectroscopy (EDS) data were collected on a traverse perpendicular to the lamellar orientation that consists of 100 points, which left a straight line of dark dots by the electron beam. Even though the dots appear to be isolated from each other in the image, they may still interfere with one another and affect the result of the analysis, which makes quantifying the composition accurately very challenging (zoomed-in image of EDS spots shown in Figure S9). The Na in the sample is more sensitive to damage from the electron beam, meaning the Na counts from the spectra have a larger uncertainty. Therefore, we plotted only the Ca count along the traverse, with each data point matched with the corresponding dark dot left in the Z-contrast image by the electron beam. Note that the absolute intensity in the EDS spectrum is dependent on the thickness of the material, which is probably the reason for the gradual increase in counts from left to right on the traverse. Nonetheless, the relative counts between adjacent points are useful for comparing the compositional difference between Ca-rich and Na-rich lamellae. The Ca counts from the EDS spectra agree very well with the contrast of the HAADF image, with more Ca in the brighter band, and less Ca in the darker ones.

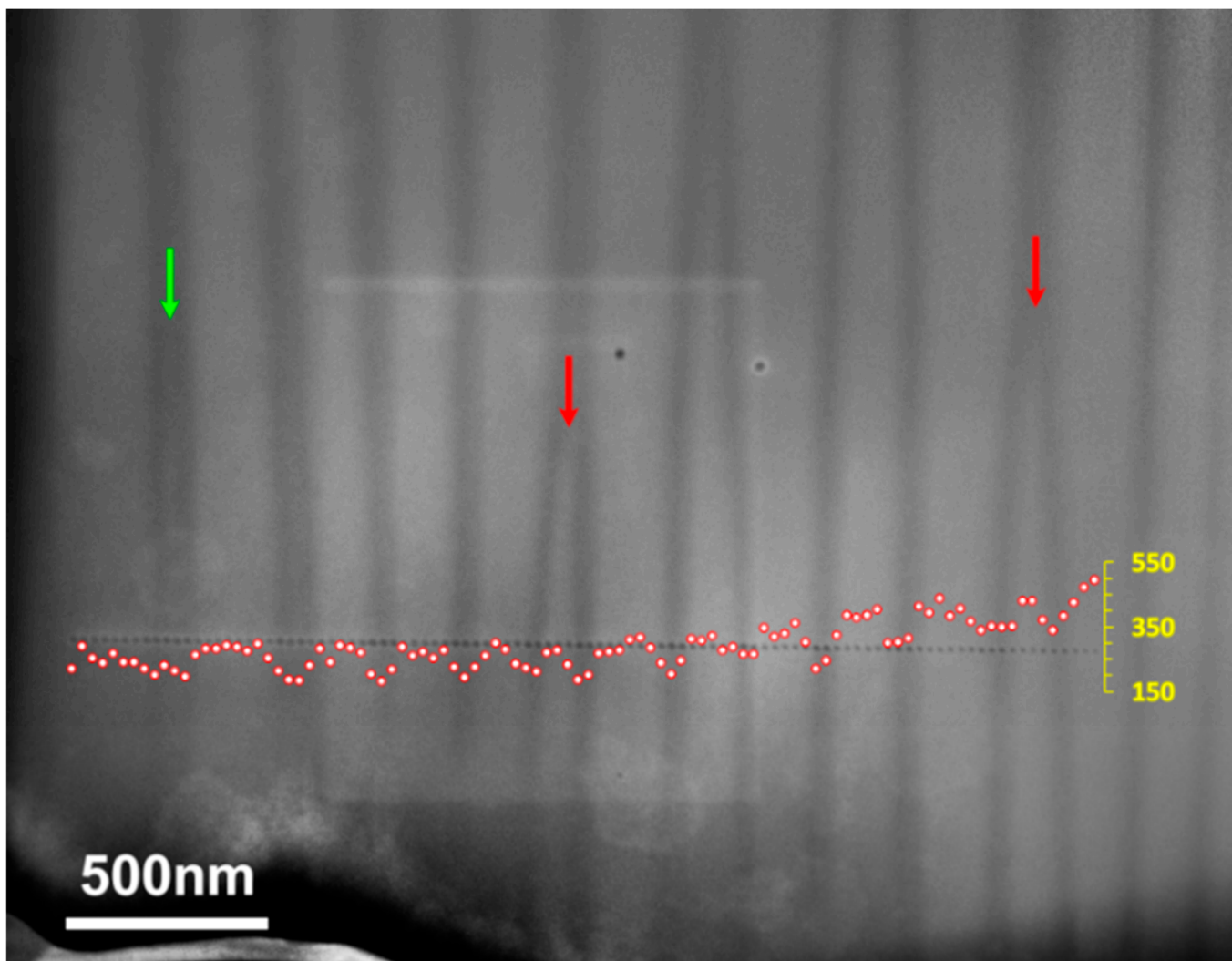


Figure 3. HAADF STEM image of sample 987L. The bright and wider lamellae are Ca-rich and the dark and thinner ones are Na-rich. EDS data are collected on a traverse across the lamellae, which left a straight line of dark dots in the image. High-resolution TEM images of the sample after electron beam damage can be found in Figure S9, which shows that the beam-damaged zones from separate spots sometimes interfere with each other. The Ca counts from the EDS spectrum are also plotted on the image, matching the marks corresponding to each data point. The green arrow marks the center of a wider Na-rich lamellae, which appears slightly more calcic. The two red arrows mark the Ca-rich lamellae wedged into branched Na-rich lamellae.

As shown in Figure 3 and Figure S9, feldspar samples are quite vulnerable under a high-energy electron beam, making point EDS analysis highly inaccurate. Previous attempts on analyzing individual lamellae in iridescent labradorite using point EDS analysis resulted in large uncertainties [6–8]. Therefore, STEM EDS mapping was applied in this study to analyze the composition of individual lamellae, minimizing the beam damage on each individual spot. Two Ca/Na maps of the red-iridescent and blue-iridescent areas of sample Gem113 are shown in Figure 4, and representative spectra extracted from two adjacent lamellae are provided in Figure 5. A higher contrast between adjacent lamellae can be seen in the map of the blue-iridescent sample compared to the red-iridescent sample, agreeing with the larger change in the orientation of the *e*-fringes across lamellar boundaries, as observed in Figure 1. EDS maps of the other igneous samples are provided in Figures S10–S13.

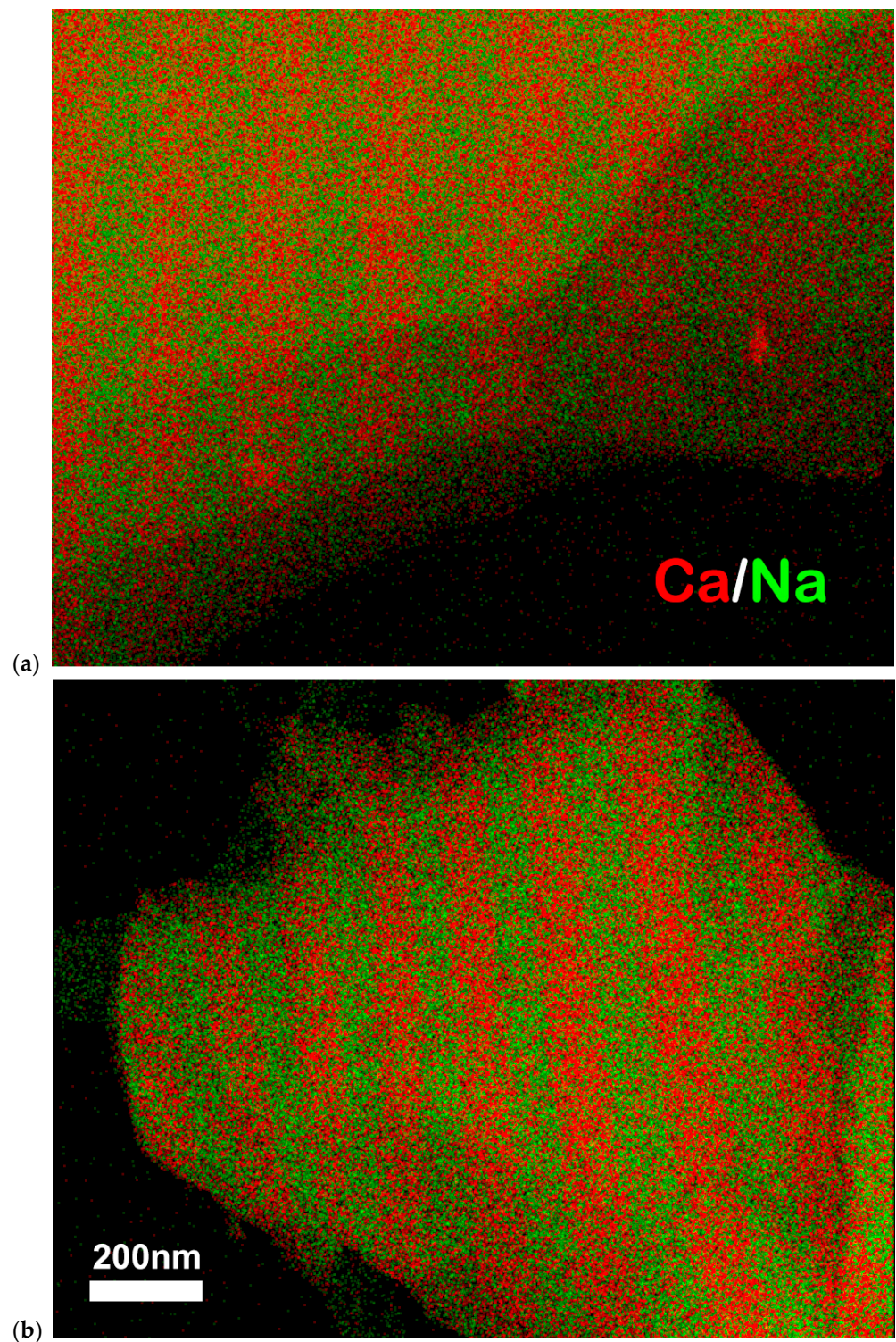


Figure 4. The Ca (red) and Na (green) EDS maps of the red-iridescent (a) and blue-iridescent (b) areas in sample Gem113. The contrast is higher in the blue-iridescent sample, indicating a larger chemical difference between the Ca-rich and the Na-rich lamellae compared to the red-iridescent sample. The magnification for both images is same.

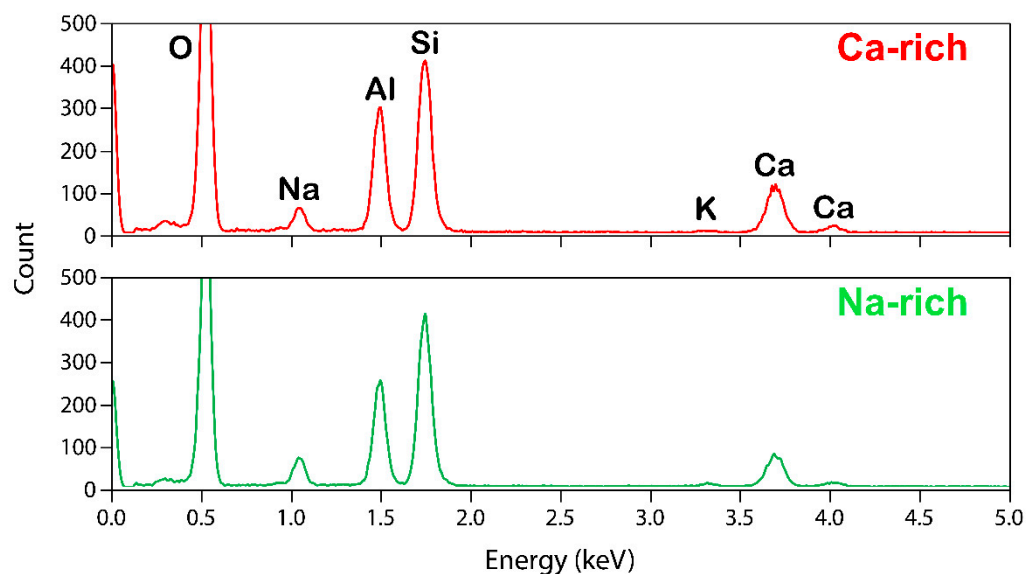


Figure 5. Representative EDS spectra of the Ca-rich and Na-rich lamellae extracted from the EDS maps in Figure 4. The spectrum from the Ca-rich lamella obviously has larger Ca/Na and Al/Si ratios than the Na-rich lamella does.

The composition of each individual lamella can be calculated following the simple equation by Lorimer and Cliff [37]:

$$\frac{I_1}{I_2} = k_{1,2} \frac{c_1}{c_2} \quad (1)$$

in which the k -factors are calculated for each adjacent lamella pair by fitting the volume ratio to an estimated value ($\sim 2:1$ for the red-iridescent areas, and $\sim 1:1$ for the blue-iridescent area) following the lever rule. The I_{Ca}/I_{Na} for Ca-rich/Na-rich lamella pairs, k -factors for each pair, An# for each lamella, and effective volume ratio that matches the bulk An# are listed in Table S2. The k -factors for lamella pairs within the same map are similar but still show some variability, and the difference between k -factors from different maps can be quite large. It is understood that the volume ratio is a rough estimation from the TEM imaging of the samples, which may introduce some uncertainties to the k -factors and lamellar compositions. The calculation of these differences between Ca-rich and Na-rich lamellae, on the other hand, are more accurate, because it is not sensitive to the volume ratio or k -factors. The resulting bulk and lamellar compositions for all the mapped samples are listed in Table 2.

Table 2. The bulk and lamellar compositions (in An#) of the iridescent labradorite samples were calculated from the EDS maps. The raw EDS intensity ratios of each lamella pair can be found in Table S2.

Sample	R2923-Blue	R2923-Red	Gem113-Blue	Gem113-Red	VB-Yellow	Gem118-Blue	Gem118-Red
Bulk An#	50.5	52.5	52	54	55	55	58
Ca-rich	58	56	59	57	58	63	63
Na-rich	44	46	45	47	48	48	48
Difference	14	10	14	10	10	15	15

3.2. Atom Probe Tomography

TEM and STEM images or EDS maps only provide two-dimensional information of the Bøggild intergrowth in iridescent labradorites, which means that the detailed information along the thickness of the lamellae is lost. Atom probe tomography is a technique that can provide 3D imaging and chemical analysis at the sub-nanometer scale. By applying voltage or laser pulses to a sharp needle-shaped material (diameter of tens of nanometers)

under high-field, atoms and/or simple molecules on the surface of the material are ionized and field-evaporated. The ions are accelerated away from the sample and hit a position-sensitive detector placed several tens of centimeters away. The mass-to-charge ratio is calculated based on the time-of-flight of the ion. A computer algorithm can be used to identify and reconstruct the ion positions in 3D with sub-nanometer resolution using the X and Y detector coordinates, and the sequence of the evaporated ions. This technique was first developed for studying metallic materials, with good conductivity and relatively simple chemistry. Nonconductive natural materials with complicated chemistry have become the subject of APT analysis more recently [38–44]. One of the complications introduced by silicates or other oxide minerals is that simple molecules ionize, in addition to single ions, which makes the identification and separation of peaks in the mass spectrum complex.

The red-iridescent and the blue-iridescent areas of sample Gem118 were selected for APT analysis. The microtip was oriented parallel to the [100] zone axis of the labradorite crystals (which includes both cleavage planes, (010) and (001)) to minimize the chance of sample breakage along cleavages. The microtips are thinner than individual lamellae of the Bøggild intergrowth, and they are oriented at a small angle with the lamellar boundaries, which means there is a high probability of the microtip not containing any lamellar boundary. Three microtips of the red-iridescent sample were analyzed before finding one that contains the lamellar boundary. All three microtips of the blue-iridescent sample show homogeneous compositions corresponding to the Ca-rich lamellae. The reconstructed Ca and Na elemental maps from APT data of the red-iridescent sample are shown in Figure 6, with the isosurfaces representing the lamellar boundary marked. The Ca/Na ratio plotted against distance perpendicular to the boundary is shown in Figure 7. A transition width of ~27 nm was calculated from the 4τ value of the sigmoid function fit of the profile [45], which agrees with the width observed in the high-resolution TEM image (Figure 1).

Species loss is a known issue for APT analysis of covalently or ionically bonded materials, especially O loss in oxides or silicates [46–49]. A recent study on feldspars also showed a strong bias toward Ca in the resulting composition [43]. Therefore, the atomic counts from the APT data cannot be directly used for calculating the feldspar compositions. The comparison among the results from different runs shows that the atomic counts are consistent between analyses on samples with the same composition, indicating that the atom counts are controlled by the properties of the sample, and they are not sensitive to the running conditions. The same method used in the EDS analysis can be used for calculating the composition from the APT data, by assuming the same principle is followed:

$$\frac{Ct_1}{Ct_2} = k_{1,2} \frac{c_1}{c_2} \quad (2)$$

in which Ct_1 and Ct_2 are the atomic counts for any two elements in the material. As O has a constant atomic percentage in all feldspars, constrained by stoichiometry, the $k_{1,O}$ values can be calculated for all the cations using the composition of the Ca-rich lamellae from the EDS maps. The resulting compositions from the APT data can be found in Table 3. The Or# was estimated from the EPMA result. The compositional difference between Ca-rich and Na-rich lamellae agrees well with the EDS analysis.

Table 3. Normalized atomic counts and corrected atom per formula of sample Gem118 from the atom probe tomography data. The k factors are calculated based on the Ca-rich lamellae from the EDS mapping. The composition of the Na-rich lamella is highlighted in green.

k_O	Lamellae	Atomic Counts Normalized by Oxygen					Corrected Atom per 8 Oxygen				
		Ca/O	Na/O	K/O	Al/O	Si/O	Ca	Na	K	Al	Si
		0.95	0.72	0.59	1.43	1.38					
Red-Gem118	Ca-rich	0.075	0.031	0.0012	0.289	0.404	0.63	0.35	0.016	1.62	2.34
	Ca-rich	0.076	0.032	0.0014	0.287	0.401	0.64	0.35	0.020	1.61	2.33
	Ca-rich	0.076	0.032	0.0021	0.292	0.410	0.64	0.36	0.028	1.63	2.38
	Na-rich	0.056	0.043	0.0029	0.264	0.434	0.47	0.48	0.040	1.48	2.52
Blue-Gem118	Ca-rich	0.075	0.031	0.0014	0.293	0.408	0.63	0.35	0.019	1.64	2.36
	Ca-rich	0.076	0.031	0.0014	0.297	0.407	0.64	0.34	0.019	1.66	2.36
	Ca-rich	0.074	0.029	0.0014	0.297	0.411	0.62	0.32	0.019	1.66	2.38

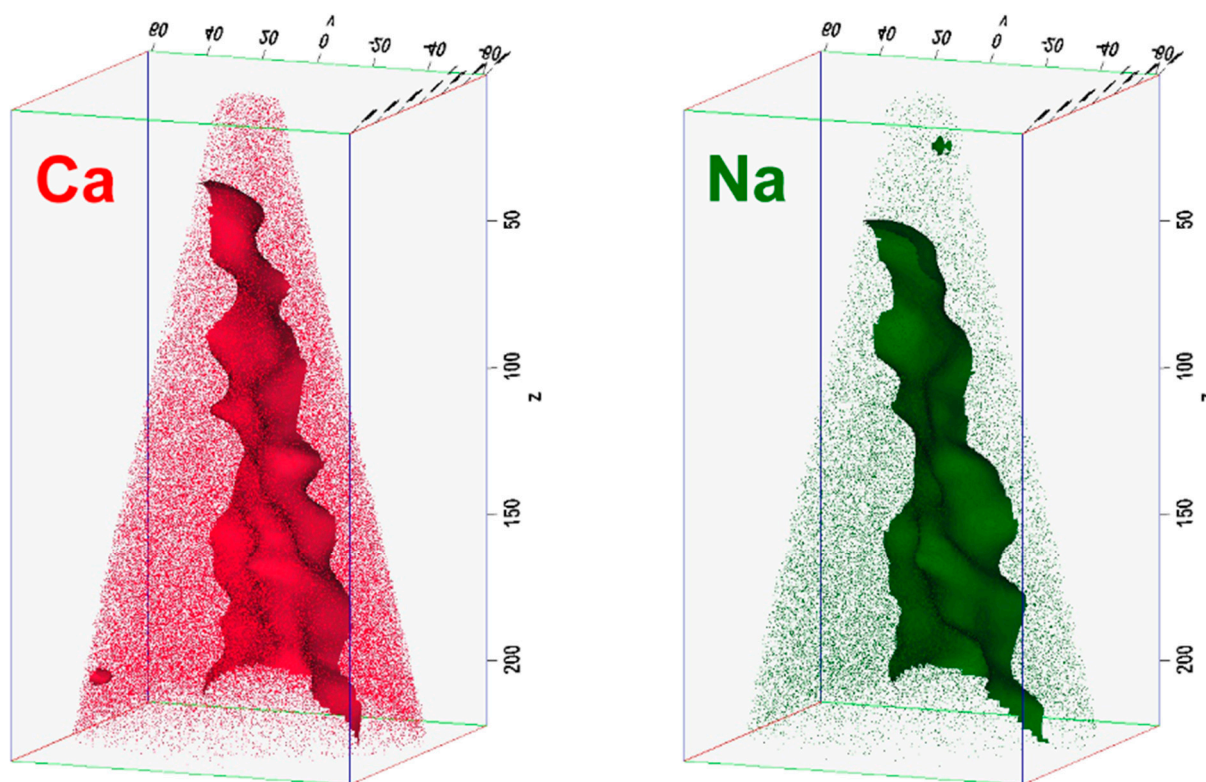


Figure 6. Ca and Na atom maps (30% displayed) from the reconstruction of the atom probe tomography data (scales in nm). No obvious change in concentration can be directly observed in the reconstruction. The isosurfaces of Ca and Na concentrations are shown in the figure as a representation of the lamellar boundary. The concentrations of Ca and Na had to be seriously smoothed with large delocalization factors; otherwise, the local fluctuation in concentrations (most likely due to the density modulation in the crystal structure) would overwhelm the difference across the lamellar boundary. The boundaries in the Ca and Na maps are very similar in detail and show similar roughness as the high-resolution TEM images in Figure 1. A movie file (gif file) showing the 3D rotations of the maps can be found in Supplementary Materials (Video S1).

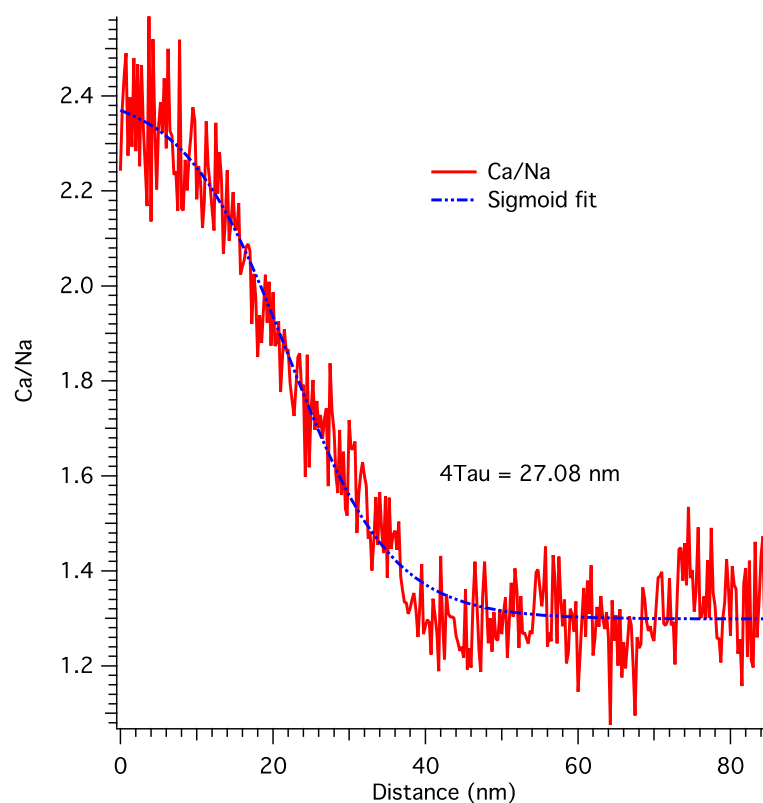


Figure 7. Ratio between Ca and Na atomic counts across the lamellar boundary. The composition changed in a relatively narrow area of less than 30 nm.

3.3. Single-Crystal X-ray Diffraction

The incommensurately modulated structures of the well-ordered *e*-labradorite crystals have been extensively described in recent papers [14,15,23,29,30], including some of the samples used in this paper. A modulated structure is a lattice periodic basic structure that is modified by a periodic modulation function. The modulated structure is incommensurate when the ratio between the modulation period and the basic unit-cell length is irrational. The incommensurately modulated structures (or aperiodic structures) are characterized by satellite reflections that cannot be indexed with three integer or rational numbers. The satellite reflections in the plagioclase structure are *e*- and *f*-reflections (first- and second-order satellites, respectively). The relative positions of the satellite reflections to the main Bragg reflections are defined by the *q*-vector in reciprocal space, which is determined by the orientation and period of the modulation function in real space. The intensities of the satellite reflections are determined by the amplitude of the modulation function.

Single-crystal X-ray diffraction is the most accurate way to measure the average *q*-vectors (modulation vectors), as well as the intensities of the satellite reflections in the diffraction pattern. Therefore, we collected diffraction data for sample Gem118 (both red-iridescent and blue-iridescent area), sample Gem113 (red-iridescent area), and sample MAD (orange-iridescent area) to compare the modulation vectors and satellite peak intensities with the structures reported in recent studies. The refined average structures show no obvious difference from previously reported iridescent *e*-labradorite (R2923, 7147A, or VB) [15,23], which means the ordering state, or the modulation amplitude, can be somewhat represented by the intensity of the (0711) peak.

The normalized (0711) intensities of all the iridescent labradorite crystals are plotted against the An# in Figure 8, along with all the data points from [23]. Most of the iridescent labradorite samples show well-ordered *e*1 structures with strong *e*-reflections comparable to those in metamorphic labradorite samples (987L and 97796b), which is expected for the extremely slow cooling rate indicated by the Bøggild intergrowth. It is also worth

noting that sample VB-colorless (An_{59}) has an obviously stronger modulation than sample VB-yellow (and most of the other iridescent labradorite crystals) with only a slightly higher $An\#$, which suggest that the exsolution process is impeding the e -ordering to some extent.

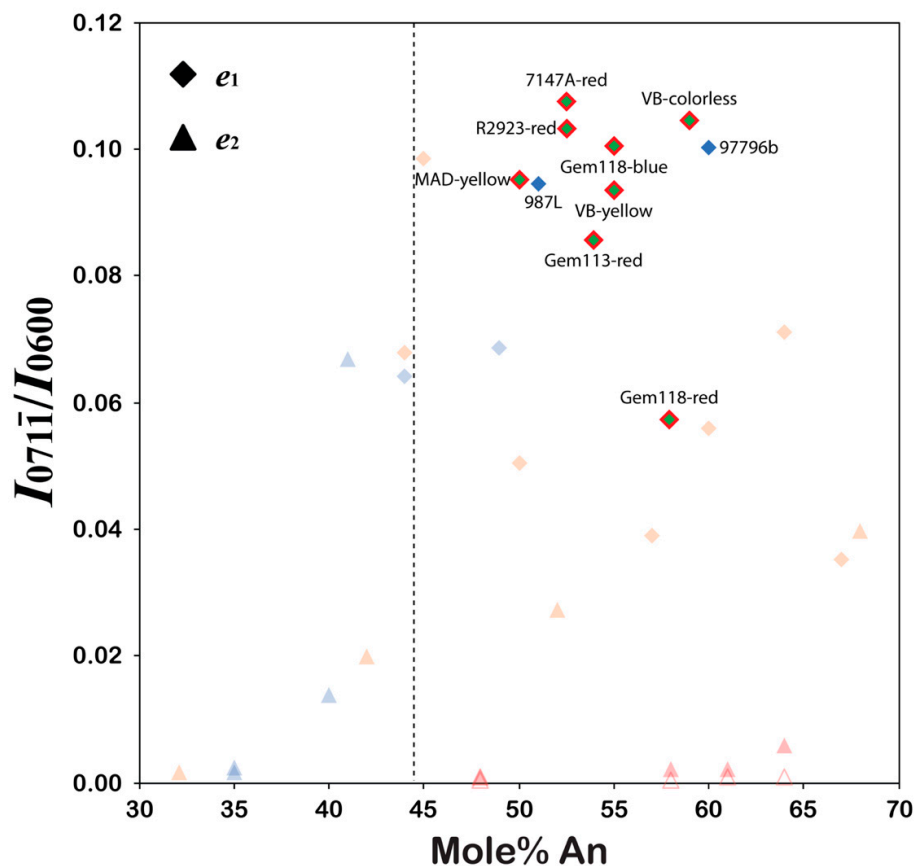


Figure 8. The normalized $(071\bar{1})$ intensities of the samples studied in this paper along with the data from [23], plotted against $An\#$ of the samples. One obvious outlier is the red Gem118 sample, which has much weaker satellite peaks compared to the other samples, especially the blue Gem118, with which it shares the same thermal history.

Unexpectedly, the normalized $(071\bar{1})$ intensity of the red-iridescent Gem118 is much weaker compared to the other iridescent labradorite structures, which is only about half that of the blue-iridescent Gem118. This is very abnormal, considering the red- and blue-iridescent areas of sample Gem118 should share exactly the same thermal history, and satellite intensity almost always increases with $An\#$ under the same conditions. The structural anomaly of the red-iridescent Gem118 is even more obviously shown in the positions of the satellite reflections, as defined by the q -vector in the reciprocal space. The satellite reflections and q -vectors of incommensurately modulated structures are usually identified by collapsing the entire reciprocal space into one single reciprocal lattice. Satellite reflections appear as small clusters next to the large cluster of main reflections at the origin of the collapsed lattice. As shown in Figure 9a,b, the satellite peaks of most iridescent labradorite crystals appear as spherical clusters, as if it is an homogeneous single crystal. This is because the X-ray beam and detector in the single-crystal X-ray diffractometer do not have the resolution to separate the small splitting of e -reflections observed in electron diffraction patterns (Figure 1). The e -reflections of red-iridescent Gem118, on the other hand, appears as two separate clusters with different sizes (Figure 9c), indicating a much larger splitting of e -reflections than the other iridescent labradorite samples. Only one cluster of f -reflections can be observed, with the same q -vector as the larger e -reflection cluster. The orientation of the q -vectors is also dramatically different from the other iridescent

labradorite, disproportionate to the difference in bulk composition. This anomaly can also be directly observed in the raw diffraction data. The unwarped $hk3h + \bar{k}$ precession images (equivalent to the [311] zone-axis diffraction patterns) of the red-iridescent Gem118 (Figure 10a) clearly show two different orientations of the e -reflection pairs, whereas the satellite peaks of the blue-iridescent Gem118 are of the same orientation (Figure 10b). The frames of X-ray diffraction data showing split e -reflections can be found in Figure S14. The q -vector of the larger e -reflection cluster, presumably diffracted by the Ca-rich lamellae, is much shorter than what is expected for the composition of $\sim\text{An}_{63}$ from the EDS and APT analysis. It is actually very close to the q -vector of sample 11044.p3, which has a composition of An_{68} [23]. During the development of Bøggild intergrowth of the red-iridescent Gem118, the e -ordering in the structure must have been strongly affected by some process that was not experienced by the other iridescent labradorite samples.

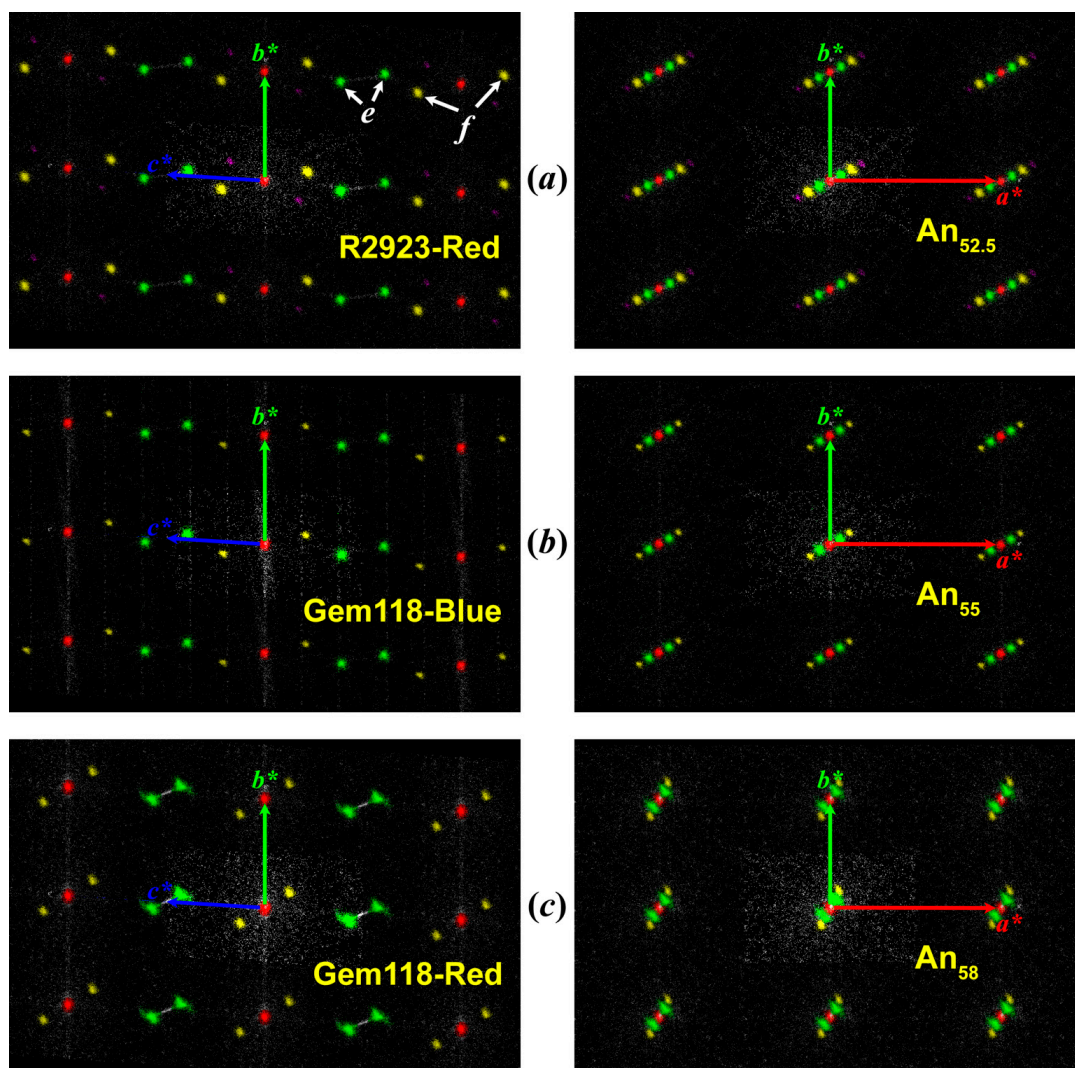


Figure 9. Comparison between the modulation vectors of the red-iridescent R2923 (a), the blue-iridescent Gem118 (b), and the red-iridescent Gem118 (c), by collapsing all the reflections in the diffraction data to the reciprocal lattice range. The blue-iridescent Gem118 shows a slightly tilted and shorter modulation vector compared to the red R2923, which agrees well with the ~ 2.5 mol% difference in their An#. The modulation vector of the red-iridescent Gem118, however, is much more tilted and shorter compared to the other sample, disproportionate to the composition difference. The e -reflections (green color) of the red-iridescent Gem118 also show two separate clusters of irregular shapes, corresponding to the two different modulation vectors, which can be observed in the precession image (Figure 10).

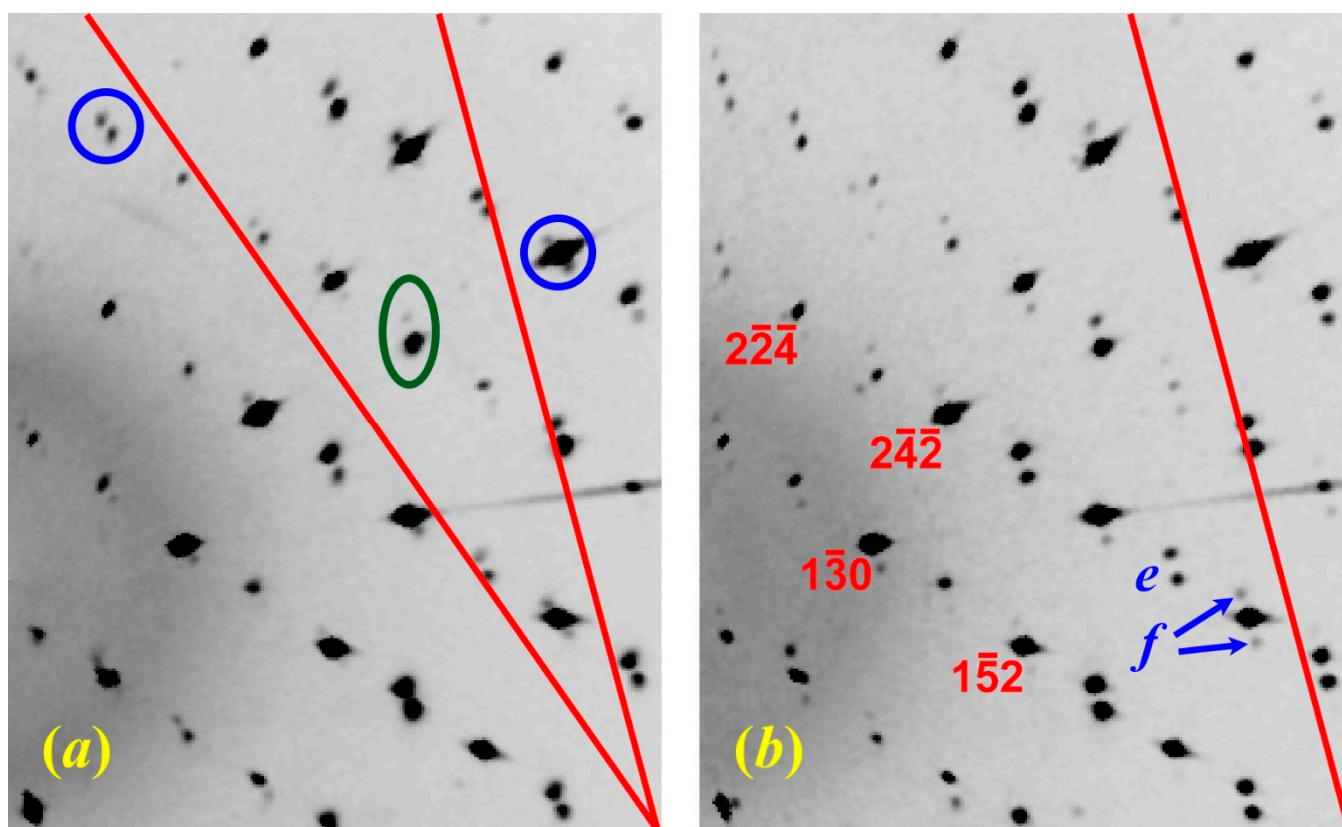


Figure 10. Unwarped $hk3h + k$ precession images (equivalent to the $[311]$ zone-axis pattern in Figure 1) of the red-iridescent (a) and blue-iridescent (b) crystals of sample Gem118. The modulation vectors in the red Gem118 (left) show two different orientations. One has a smaller tilt angle similar to that of the blue sample, represented by the e -reflections marked by the green ellipsoid. The other has a much larger tilt angle and smaller separation, represented by the e - and f -reflections marked by the blue circles. Unprocessed diffraction frames showing the split e -reflections can be found in Figure S14.

4. Discussion

Four different phases with different crystal structures can be found within the compositional range of the Bøggild intergrowth, which is the main reason why the phase relations around the Bøggild intergrowth are so complicated. Equilibrium for low temperatures is impossible to achieve within a reasonable timescale in the lab experiments, thanks to the extremely slow CaAl-NaSi interdiffusion rate [50,51], and detailed thermal histories of natural samples are hard to constrain. The subsolidus phase relations of plagioclase feldspar solution has been most comprehensively summarized by Carpenter [13] (Figure S16), taking into consideration all the reported experimental data and natural samples available at the time. There are, however, some inconsistencies between the labradorite region in Carpenter's phase diagram and some recent discoveries regarding the incommensurately modulated structures of e -plagioclase [14,15,23,29,30,32]. The new data reported in this paper regarding the Bøggild intergrowth also provide some new insights to the subsolidus phase relations of the low-temperature intermediate plagioclase, as is discussed below.

The first phase relation to be discussed is that between the $e1$ and $e2$ phases. Recent studies [15,23,30,32] have shown that the $e2$ structure can be ordered into the $e1$ structure continuously, and a second-order phase boundary has been proposed between An_{40} and An_{44} at below 550 °C. A small discontinuity is also possible, as suggested by the abrupt change in the q -vectors in sample H4-04 between An_{44} and An_{45} [29,30]. The homogeneous metamorphic $e1$ structure with a composition of An_{52} [14] and the igneous $e1$ structures with compositions as sodic as An_{42} [30] all suggest a continuous region of the $e1$ phase bounded

by a inclined gap with the $C\bar{1}$ phase, which was first proposed by McConnell [12,26] and was adopted by the phase relations in Jin et al. [23].

Carpenter [13] proposed the Bøggild intergrowth to be coexisting $e1$ and $e2$ structures at low temperature, but acknowledged that the $C\bar{1}/e1$ Bøggild gap that closes at low temperature remains a possibility. Most TEM images showing the e - or f -fringes across the lamellar boundaries are inconclusive about the structure state of the Na-rich lamellae [2,11,35,36]. However, the synchrotron X-ray diffraction data of an iridescent labradorite [22] provide some more definitive evidence supporting that the Na-rich lamellae are of the $e1$ phase, with obvious f -reflections (which are misnamed $e2$ reflections in [22]) appearing in both lamellae, as indicated by the pear-shaped distribution of the satellite peaks.

The compositional analyses of individual lamellae in this work further argue against the Bøggild gap almost symmetrical around An_{50} by Carpenter [13] (Figure S16C), which is based on the equal volume proportion observed in iridescent labradorite samples of $\sim An_{50}$. However, sample 987L with almost the same composition ($\sim An_{49}$) shows an intergrowth texture dominated by Ca-rich lamellae (>80%) (Figure 3); the blue-iridescent Gem118 with a more calcic composition (An_{55}), on the other hand, shows equal volume between Ca-rich and Na-rich lamellae (Figures S3 and S10). These indicate that the volume ratio of lamellae is not only dependent on the bulk composition of the sample, but also strongly depends on the thermal history. The compositions of the Ca-rich lamellae from different samples show a much larger variation than the compositions of the Na-rich lamellae (Table 2), which also support an asymmetrical gap shifting toward the albite side at low temperature. The anti-correlation between the lamellar thickness and the composition difference in sample R2923 and Gem113 (blue-iridescent zone with thinner lamellae shows a larger composition difference between Ca-rich and Na-rich lamellae, relative to the red-iridescent zone with thicker lamellae) also cannot be explained by the symmetrical shape of the Bøggild gap proposed by Carpenter [13]. Therefore, the symmetrical Bøggild gap as coexisting $e1$ and $e2$ structures is not further considered in this paper. The boundary between $e1$ and $e2$ phase is drawn as a straight line following [23].

There is another issue with the phase diagram proposed by Carpenter [13], which depicted the $I\bar{1}/e1$ boundary to be continuous at high temperature (~ 800 °C) before expanding to the Huttenlocher gap with more calcic compositions. The schematic free-energy curves are also drawn with the $e1$ phase continuously merged to the $I\bar{1}$ phase on the anorthite side. These are based on an incorrect structure model of the e -plagioclase structure, and an incorrect understanding of the superspace group symmetry of the e -plagioclase. The $X\bar{1}(\alpha, \beta, \gamma)0$ superspace group is a subgroup of $C\bar{1}$, but not a subgroup of $I\bar{1}$. It is symmetrically not possible to continuously transform a $I\bar{1}$ structure to an e -plagioclase ($X\bar{1}(\alpha, \beta, \gamma)0$) without going through the disordered $C\bar{1}$ as an intermediate stage [23], despite the experimental data seemingly suggesting a continuous transition [52–54]. The various e - and b -reflections observed in synthetic anorthite by Carpenter [55] should be interpreted as the metastable $C\bar{1}/e2$ transition occurring with a short anneal time, before the $C\bar{1}/I\bar{1}$ transition takes over with a longer anneal time, suggesting that the $e2$ ordering is kinetically favorable with the $C\bar{1}$ structure, albeit thermodynamically less stable [15,31,32]. The misconception of the relationship between $I\bar{1}$ and e -plagioclase seems to have mainly stemmed from the similarity in diffraction pattern, where the e -reflections are intuitively viewed as a “splitting” of the elongated b -reflections. It should be noted though that a seemingly continuous transition in reciprocal space does not necessarily correspond to a continuous transition in real space. A “splitting” of the b -reflection into e -reflections would mean a transition from an infinite modulation period to a finite period, which cannot be continuous. Therefore, the phase transformation between $I\bar{1}$ and $e1$ cannot possibly be continuous at any composition, and the G-X free-energy curve of the two phases can only intercept but may never merge.

The discontinuity between $I\bar{1}$ and $e1$ structures also means that the stable regions of the three phases ($C\bar{1}$, $I\bar{1}$, and $e1$) meeting at one single point, as proposed by Carpenter [13], is not possible. The topology of the boundaries among the three phases has to be more

complicated with three separate free-energy curves for each phase. As suggested by [23], the boundary between $I\bar{I}$ and $e1$ should be simple, with a negative slope between temperature and An#, which widens up to the Huttenlocher gap at lower temperature. The question is how it might intersect with the $C\bar{I}/I\bar{I}$ boundary or the $C\bar{I}/e1$ gap. There are a few possibilities depending on the shape of the free-energy curves of $I\bar{I}$ and $e1$ as a function of An# (G-X curves) at different temperatures. The simplest cases of the schematic G-X curves and corresponding phase relations are illustrated in Figures 11 and 12, respectively. It should be noted that the phase relations presented in Figure 12 are mainly to show the topology of the phase areas and boundaries of the different phases. Without new experimental data, it is impossible to constrain the exact phase transition temperatures better than Carpenter [13]. The simplest convex G-X curve for the $I\bar{I}$ phase (Figure 11a) would result in a phase topology shown in Figure 12a, in which there are two miscibility gaps between the $I\bar{I}$ and $e1$ phase, both terminating at the same point where the G-X curve of $e1$ is tangent to that of $I\bar{I}$. This phase topology is highly unlikely, because it rules out spinodal decomposition as a forming mechanism of the Bøggild intergrowth for compositions more calcic than An₅₀. A slight change in the G-X curve (Figure 11b) would result in a miscibility gap within the $I\bar{I}$ phase (Figure 12b), which was first suggested by Smith [5]. The calculated G-X curve by Carpenter [53] also suggests a solvus within the $I\bar{I}$ phase. This topology was adopted in the phase diagram by [23] and may explain the intergrowth between An₆₁ and An_{69.5} found in plagioclase from a gneiss [56].

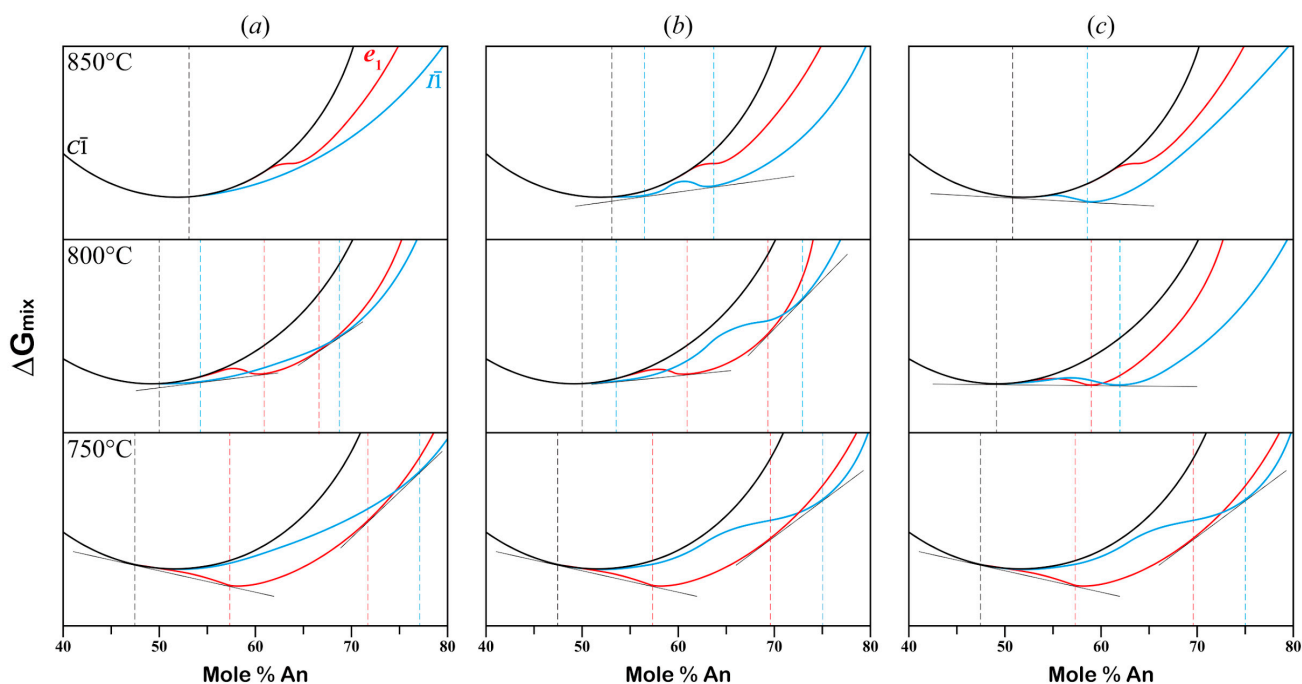


Figure 11. Schematic G-X curves of the $C\bar{I}$ (black), $e1$ (red), and $I\bar{I}$ (cyan) phases around the $I\bar{I}/e1$ transition temperature. (a) The $I\bar{I}$ curve is of a simple convex shape within the composition and temperature range; (b) the $I\bar{I}$ curve results in a solvus within the $I\bar{I}$ phase; (c) the $I\bar{I}$ curve results in a coexisting area between the $C\bar{I}$ and the $I\bar{I}$ structures.

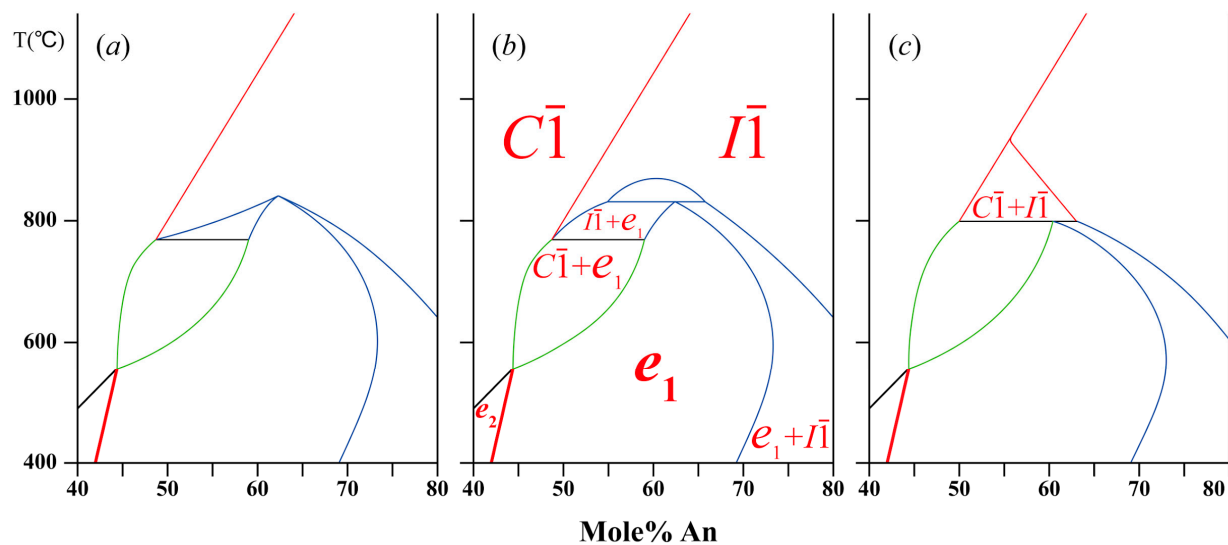


Figure 12. The schematic phase relations around the Bøggild gap showing the topology among the different phase regions, corresponding to the different G-X curves shown in Figure 11. (a–c) are corresponding to the cases of (a–c) of Figure 11, respectively.

The scenarios discussed above are restricted by the $C\bar{1}/I\bar{1}$ boundary being a continuous straight line that extends all the way down to An_{50} at ~ 800 °C. However, no $I\bar{1}$ structure less calcic than An_{55} has been reported, either in natural samples or in experiments. A recent structure study showed that the $C\bar{1}/I\bar{1}$ transition is much harder kinetically compared to the $C\bar{1}/e_2$ transition, even though the energy barrier for Al-Si ordering should be very similar, which suggests that the $C\bar{1}/I\bar{1}$ boundary may not be as continuous as previously believed [31,32]. This opens up another possibility where the $C\bar{1}/I\bar{1}$ opens up to a miscibility gap between two phases below ~ 900 °C. As a matter of fact, a slightly different shape of the $I\bar{1}$ curve from Carpenter [53] could result in a coexisting area between $C\bar{1}$ and $I\bar{1}$ (Figure 12c). This possibility was first proposed by Smith [24], and further discussed by Grove et al. [27]. The computational study by [57] also supported a first-order boundary between $C\bar{1}$ and $I\bar{1}$ structures. The *b*-reflection dark-field images in [58,59] were interpreted to be the evidence for conditional spinodal decomposition between $C\bar{1}$ and $I\bar{1}$ [27]. Intergrowth between the $C\bar{1}$ and $I\bar{1}$ structures with larger domains may never be found in nature, because any rock that cooled slow enough to develop coarse textures would certainly order into e_1 structures at lower temperature. Other possible topologies than those illustrated in Figure 12 would require more complicated shapes in energy curves, or unlikely coincidences relating the energy curves of different phases would, therefore, not be considered in this paper without any evidence.

The formation mechanism of the exsolution lamellae in the Bøggild intergrowth should be briefly addressed here. All the iridescent labradorite samples found in nature behave quite similarly, with lamellar thicknesses at the same scale, which do not provide enough variations, possibly resulting from different cooling histories. The exsolution textures in alkali feldspars, on the other hand, occur within a much shorter time scale, and have been intensively studied experimentally, which may provide some clues for the forming mechanism of the Bøggild intergrowth. The formation mechanisms of the exsolution textures in perthites are best summarized by [60]. The Bøggild intergrowth has always been believed to be formed through spinodal decomposition, given the regularity in lamellar orientation and thickness [2,5,13,26]. Nucleation and growth, however, are also known to produce similar textures in micro-/crypto-perthites [60], and should not be totally ruled out. A definitive distinction between the two possible forming mechanisms would require a scrutiny in the terminations of both the Ca-rich and Na-rich lamellae over a large area, which would be quite challenging considering the 2-D nature of the lamellae. The large-area image in Smith and Brown [5] (their Figure 19.30a) seemed to only show

wedge-shaped terminations in the major lamellae, and branches in the minor lamellae, suggesting a possible nucleation and growth mechanism. The exsolution lamellae in sample 987L shown in Figure 3 also only show wedge-shaped terminations of the Ca-rich lamellae (marked by red arrows) in an area a few micrometers across. Some Na-rich lamellae appear to be slightly more calcic toward the center (Figure 3 and Figure S12), which could match the residue diffusion profile resulting from nucleation and growth of the Ca-rich lamellae [60]. On the other hand, the composition profile across the lamellar boundary from the APT analysis of sample Gem118 shows the composition within each lamella to be quite homogeneous, with a smooth transition across the boundary. Assuming the lamellae in Gem118 were produced by spinodal decomposition, this profile is characteristic of the final stage when a sharp interface is developed with the lamellar compositions lying on the coherent miscibility gap. The blue- and red-iridescent areas of sample Gem118 having the same lamellae compositions also suggest equilibrium at a certain temperature. The other iridescent labradorite samples, however, show different lamellar compositions between the blue- and red-iridescent zones, suggesting disequilibrium during the lamellae development. Detailed composition profiles from more iridescent labradorite samples, perhaps with APT analysis or ion-beam depth profiling, might provide more information about the formation process and mechanism of the Bøggild intergrowth. It is quite possible that both spinodal decomposition and nucleation and growth could form the Bøggild intergrowth, depending on compositions and thermal histories.

The structural anomaly observed in the red-iridescent Gem118 is quite surprising. Some type of phase boundary must exist between An_{55} and An_{58} , in order to allow the two different zones within the same crystal to go through different ordering processes under the same thermal conditions. The blue-iridescent Gem118 developed the $e1$ structure similar to the other iridescent labradorite samples, suggesting that they experienced similar phase behaviors, whereas the red-iridescent Gem118 went through a different process that inhibited and modified the e -ordering process significantly. The most plausible boundary that could cause this difference is the transition from $C\bar{1}$ to $I\bar{1}$, given the possible topologies of the phase relations illustrated in Figure 12. The absence of density modulation in the structure of 11044.p3 (An_{68}) [23] has suggested that the transformation to the $I\bar{1}$ structure could inhibit the $e1$ ordering. Carpenter [13] also suggested that crystals on either side of the intersection between the $C\bar{1}/I\bar{1}$ boundary and Bøggild gap would go through different phase paths during cooling. However, the variations in e - or f -fringes across the lamellar boundaries in TEM images were incorrectly interpreted as evidence to support this claim, because the variation in 3D modulated structures may not be reflected in the 2D projection in a TEM image, depending on the sample orientation relative to the electron beam. Based on the composition of sample Gem118, the intersection between the $C\bar{1}/I\bar{1}$ gap and the Bøggild gap in Figure 12a should be between An_{55} and An_{58} , which would require moving up the intersection with the $C\bar{1}/e1$ gap to at least 900 °C. This would be hard to reconcile with the transition temperature between $I\bar{1}$ and $e1$ at around 800 °C, as suggested by the experimental results [61]. The topology in Figure 12a would also mean that the exsolution lamellae in red-iridescent labradorite would be formed through $e1$ nucleation and growth within the $I\bar{1}$ host, which contradicts the wedge-shaped termination of a Na-rich lamella observed in the STEM image (Figure S11). The topology shown in Figure 12c increases the temperature at the top of the Bøggild gap by having a coexisting area between $C\bar{1}$ and $I\bar{1}$, without increasing the transition temperature between $I\bar{1}$ and $e1$, and it would allow spinodal decomposition for the entire Bøggild gap. Nonetheless, there is no obvious explanation to the strange q -vector of the $e1$ structure in the Ca-rich lamellae of the red-iridescent Gem118.

The effect of K remains elusive in the subsolidus phase relations of labradorite feldspar. It was believed in the early days that the K content in the labradorite crystals is critical to the formation of the Bøggild intergrowth [5], as all iridescent labradorites are found to have at least 2% of orthoclase component in their compositions. This was disproved when exsolution lamellae were found in a metamorphic plagioclase of An_{49} with almost

no K in the composition [62], which is further supported by the exsolution lamellae in sample 987L (Figure 3). Many igneous labradorite crystals are found with ~2% of Or in their compositions, with or without iridescent color [15,23,31,32,61–63]. There is no evidence suggesting any correlation between Or# and Bøggild intergrowth. It is known that a small amount of anorthite can change the solvus temperature in alkali feldspars dramatically [64], which is mainly caused by the extra charge of the Ca^{2+} that needs to be balanced by the extra Al in the tetrahedral framework. K in plagioclase is unlikely to play a role as dramatic as Ca in alkali feldspar, given that it has the same charge as Na and would not change the chemistry of the tetrahedral framework. The complicated phase relation of plagioclase mostly arises from the different Al-Si ordering pattern in the framework of different compositions [13]. K-feldspar precipitates have been reported in the Finland labradorite [65], which appears to have happened after the Bøggild intergrowth was already developed, based on the cross-cutting relationship in the crystal. It is worth noticing, however, the difference in the Or content between the Ca-rich and Na-rich lamellae. From the APT analyses (Table 3) and EDS maps (Figure S10), the K in the Na-rich lamellae is about twice as much as that in the Ca-rich lamellae, consistent with the ion probe result by [9]. The difference in Or# is disproportionate to the difference in An# between the Ca-rich and Na-rich lamellae, which seems to suggest that the partition of K between lamellae is affected by the structure state at the time of exsolution. The K atoms prefer the disordered $\bar{C}1$ structure over the ordered $\bar{I}1$ or $e1$ structure. The proposed phase relationship (Figure 12c) explains the observed composition distribution of plagioclase feldspars in amphibolite facies rocks reported by Wenk et al. (1979) [66]. A complete binary phase diagram of the plagioclase feldspar is proposed in Supplementary Materials (Figure S15) for comparison.

5. Conclusions

Structure and chemical analyses of labradorites with Bøggild intergrowth in this paper showed that the subsolidus phase relations of intermediate plagioclase may be more complicated than previously expected. This is the first time that the chemical composition of individual lamellae has been analyzed for different color zones within the same crystal. The compositions of Ca-rich and Na-rich lamellae not only depend on the bulk composition of the sample, but also vary significantly with different thermal histories, which cannot be explained by the symmetrical miscibility gap proposed by Carpenter [13]. Most of the previous studies on Bøggild intergrowth have treated iridescent labradorite samples from different localities as if they are the same or very similar, and lamellar compositions from different samples have been averaged to obtain the composition range of the miscibility gap [9]. The results in this work showed that the averaged composition from different samples is meaningless, and each sample represents a unique thermal history and should be examined separately.

Conventional TEM is best used for the preliminary screening of samples, due to the relatively simple sample preparation. Analytical STEM with EDS is shown to be valuable in analyzing individual lamellar compositions. Single-crystal XRD is critical in revealing details about the incommensurately modulated structures of *e*-plagioclase, even though it mostly shows the average of two structures with different compositions. Without single-crystal XRD, the anomaly that implies a phase boundary in sample Gem118 would have been missed. The high-resolution 3D composition profile across the lamellar boundaries would require more consuming techniques such as APT or secondary ion mass spectroscopy (SIMS), but might be necessary in discerning the different forming mechanisms or equilibrium conditions.

Perhaps the result in this paper raises more questions about the Bøggild intergrowth than it answers, but that is simply a reflection of how complicated the phase relations of plagioclase actually are. A few possible topologies of the phase relations around the Bøggild gap were proposed based on the simple shapes of the free-energy curve, which requires careful examinations of more labradorite samples, including some previously studied ones,

to further constrain. Metamorphic labradorite crystals seem to behave differently from the iridescent igneous labradorite crystals, likely due to the difference in thermal history, which could provide important information. Metamorphic labradorite with a peak temperature above 700 °C, in particular, may be critical in refining the subsolidus phase diagram of the plagioclase solid solution.

Supplementary Materials: The following are available online at <https://www.mdpi.com/article/10.3390/min11070727/s1>, Figures S1 and S2: Optical images of the samples studied, Figures S3–S9: TEM images of the samples studied, Figures S10–S13: STEM EDS maps of the samples studied, Figure S14: Single-crystal XRD frames from red-iridescent Gem118, Figure S15: Proposed phase diagram for plagioclase feldspars, Figure S16: Previously proposed phase diagrams for plagioclase feldspars, Table S1: EPMA analysis results of the samples studied, Table S2: Lamellar compositions from EDS spectra, Video S1: Rotation of the reconstructed 3D Ca and Na maps from the APT data. CIF: Average crystal structures refined from single-crystal XRD data.

Author Contributions: Conceptualization, H.X. and S.J.; methodology, H.X.; formal analysis, S.J. and S.L.; investigation, S.J.; data curation, S.J.; writing—original draft preparation, S.J.; writing—review and editing, H.X. and S.L.; supervision, H.X.; project administration, H.X.; funding acquisition, H.X. All authors have read and agreed to the published version of the manuscript.

Funding: This study is supported by National Science Foundation (grant No. EAR-1530614).

Data Availability Statement: The data presented in this study are available on request from the corresponding author. All the samples used in this study are deposited at the geology museum at the University of Wisconsin-Madison.

Acknowledgments: The authors thank Jianguo Wen of the Center for Nanoscale Materials of Argonne National Laboratory, and Yiping Yang of the Guangzhou Institute of Geochemistry, Chinese Academy of Science for collecting STEM images and X-ray EDS maps. Atom probe tomography (APT) analysis was conducted at ORNL's Center for Nanophase Materials Sciences (CNMS), which is a U.S. DOE Office of Science User Facility. The authors would like to thank Jonathan D. Poplawsky for collecting and processing the APT data, and James Burns for help with APT sample preparation and experiments. We thank Tyler Blum for helping us with the visualization of the APT data. The authors also thank Michael Carpenter and two anonymous reviewers for their constructive comments and suggestions.

Conflicts of Interest: The authors declare no conflict of interest.

References

1. Rose, G. Über Den Feldspat, Albit, Labradorit Und Anorthit. *Ann. Phys. Chem.* **1823**, *73*, 175–208. [[CrossRef](#)]
2. Ribbe, P.H. Exsolution textures in ternary and plagioclase feldspars; interference colors. In *Feldspar Mineralogy*; Ribbe, P.H., Ed.; Reviews in Mineralogy; Mineralogical Society of American: Washington, DC, USA, 1983; pp. 241–270.
3. Strutt, R.J. Studies of Iridescent Colour and the Structure Producing It. III. The Colours of Labrador Felspar. *Proc. R. Soc. Lond. Ser. A* **1923**, *103*, 34–45.
4. Bøggild, O.B. On the Labradorization of the Feldspars. 1924. Available online: <http://gymarkiv.sdu.dk/MFM/kdvs/mfm%201-9/mfm-6-3.pdf> (accessed on 2 July 2021).
5. Smith, J.V.; Brown, W.L. *Feldspar Minerals*; Springer: Berlin/Heidelberg, Germany, 1988; ISBN 0-387-17692-6.
6. Nissen, H.-U.; Champness, P.E.; Cliff, G.; Lorimer, G.W. Chemical Evidence for Exsolution in a Labradorite. *Nat. Phys. Sci.* **1973**, *245*, 135–137. [[CrossRef](#)]
7. Cliff, G.; Champness, P.E.; Nissen, H.-U.; Lorimer, G.W. Analytical Electron Microscopy of Exsolution Lamellae in Plagioclase Feldspars. In *Electron Microscopy in Mineralogy*; Wenk, H.R., Ed.; Springer: Berlin/Heidelberg, Germany, 1976; pp. 258–265. ISBN 978-3-642-66196-9.
8. Hoshi, T.; Tagai, T.; Suzuki, M. Investigations on Bøggild Intergrowth of Intermediate Plagioclase by High Resolution Transmission Electron Microscopy. *Z. Krist. Cryst. Mater.* **1996**, *211*, 879–883. [[CrossRef](#)]
9. Miúra, Y.; Tomisaka, T. Ion Microprobe Mass Analysis of Exsolution Lamellae in Labradorite Feldspar. *Am. Mineral.* **1978**, *63*, 584–590.
10. Olsen, A. Lattice Parameter Determination of Exsolution Structures in Labradorite Feldspars. *Acta Crystallogr. Sect. A* **1977**, *33*, 706–712. [[CrossRef](#)]
11. McConnell, J.D.C. Electron-optical study of the fine structure of a schiller labradorite. In *The Feldspars*; MacKenzie, W.S., Zussman, J., Eds.; Manchester University Press: New York, NY, USA, 1974; pp. 478–490.

12. McConnell, J.D.C. Analysis of the time-temperature-transformation behaviour of the plagioclase feldspars. In *The Feldspars*; MacKenzie, W.S., Zussman, J., Eds.; Manchester University Press: New York, NY, USA, 1974; pp. 460–477.
13. Carpenter, M.A. Subsolidus phase-relations of the plagioclase feldspar solid-solution. In *Feldspars and Their Reactions*; Parsons, I., Ed.; Kluwer Academic Publishers: Dordrecht, The Netherlands, 1994; Volume 421, pp. 221–269. ISBN 0258-2023.
14. Jin, S.; Xu, H. Solved: The Enigma of Labradorite Feldspar with Incommensurately Modulated Structure. *Am. Mineral.* **2017**, *102*, 21–32. [[CrossRef](#)]
15. Jin, S.; Xu, H. Study on Structure Variations of Incommensurately Modulated Labradorite Feldspars with Different Cooling Histories. *Am. Mineral.* **2017**, *102*, 1328–1339. [[CrossRef](#)]
16. Toman, K.; Frueh, A.J. On the Origin of Plagioclase Satellite Reflections. *Acta Crystallogr. Sect. B* **1971**, *27*, 2182–2186. [[CrossRef](#)]
17. Toman, K.; Frueh, A.J. Intensity Averages of Plagioclase Satellites: Distribution in Reciprocal Space. *Acta Crystallogr. Sect. B* **1972**, *28*, 1657–1662. [[CrossRef](#)]
18. Toman, K.; Frueh, A.J. Modulated Structure of an Intermediate Plagioclase. I. Model and Computation. *Acta Crystallogr. Sect. B* **1976**, *32*, 521–525. [[CrossRef](#)]
19. Toman, K.; Frueh, A.J. Modulated Structure of an Intermediate Plagioclase. II. Numerical Results and Discussion. *Acta Crystallogr. Sect. B* **1976**, *32*, 526–538. [[CrossRef](#)]
20. Horst, W.; Tagai, T.; Korekawa, M.; Jagodzinski, H. Modulated Structure of a Plagioclase An_{52} : Theory and Structure Determination. *Z. Krist. Cryst. Mater.* **1981**, *157*, 233–250. [[CrossRef](#)]
21. Yamamoto, A.; Nakazawa, H.; Kitamura, M.; Morimoto, N. The Modulated Structure of Intermediate Plagioclase Feldspar $Ca_xNa_{1-x}Al_{1+x}Si_{3-x}O_{3-x}$. *Acta Crystallogr. Sect. B* **1984**, *40*, 228–237. [[CrossRef](#)]
22. Boysen, H.; Kek, S. The Modulated Structure of Labradorite. *Z. Krist. Cryst. Mater.* **2015**, *230*, 23–36. [[CrossRef](#)]
23. Jin, S.; Xu, H.; Wang, X.; Jacobs, R.; Morgan, D. The Incommensurately Modulated Structures of Low-Temperature Labradorite Feldspars: A Single-Crystal X-ray and Neutron Diffraction Study. *Acta Crystallogr. Sect. B* **2020**, *76*, 93–107. [[CrossRef](#)] [[PubMed](#)]
24. Smith, J.V. *Feldspar Minerals*; Springer: Berlin, Germany; New York, NY, USA, 1974; ISBN 0387064907.
25. Smith, J.V. Phase relations of plagioclase feldspars. In *Feldspars and Feldspathoids*; Brown, W.L., Ed.; Reidel Publishing Company: Dordrecht, The Netherlands, 1984; Volume 137, pp. 55–94. ISBN 94-015-6931-2.
26. McConnell, J.D.C. The Origin and Characteristics of the Incommensurate Structures in the Plagioclase Feldspars. *Can. Mineral.* **2008**, *46*, 1389–1400. [[CrossRef](#)]
27. Grove, T.L.; Ferry, J.M.; Spear, F.S. Phase Transitions and Decomposition Relations in Calcic Plagioclase. *Am. Mineral.* **1983**, *68*, 41–59.
28. Grove, T.L.; Ferry, J.M.; Spear, F.S. Phase Transitions in Calcic Plagioclase: A Correction and Further Discussion. *Am. Mineral.* **1986**, *71*, 1049–1050.
29. Xu, H.; Jin, S.; Noll, B.C. Incommensurate Density Modulation in a Na-Rich Plagioclase Feldspar: Z-Contrast Imaging and Single-Crystal X-ray Diffraction Study. *Acta Crystallogr. Sect. B* **2016**, *72*, 904–915. [[CrossRef](#)] [[PubMed](#)]
30. Jin, S.; Xu, H. Investigations of the Phase Relations among $e1$, $e2$ and $C\bar{1}$ Structures of Na-Rich Plagioclase: A Single-Crystal X-ray Diffraction Study. *Acta Crystallogr. Sect. B* **2017**, *73*, 992–1006. [[CrossRef](#)]
31. Jin, S.; Wang, X.; Xu, H. Revisiting the $\bar{1}\bar{1}$ Structures of High-Temperature Ca-Rich Plagioclase Feldspar—A Single-Crystal Neutron and X-ray Diffraction Study. *Acta Crystallogr. Sect. B* **2018**, *74*, 152–164. [[CrossRef](#)]
32. Jin, S.; Xu, H.; Wang, X.; Zhang, D.; Jacobs, R.; Morgan, D. The Incommensurately Modulated Structures of Volcanic Plagioclase: Displacement, Ordering and Phase Transition. *Acta Crystallogr. Sect. B* **2019**, *75*, 643–656. [[CrossRef](#)] [[PubMed](#)]
33. Ferry, J.M. A Case Study of the Amount and Distribution of Heat and Fluid during Metamorphism. *Contrib. Mineral. Petrol.* **1980**, *71*, 373–385. [[CrossRef](#)]
34. Petříček, V.; Dušek, M.; Palatinus, L. Crystallographic Computing System JANA2006: General Features. *Z. Krist. Cryst. Mater.* **2014**, *229*, 345–352. [[CrossRef](#)]
35. Wenk, H.-R.; Nakajima, Y. Structure, Formation, and Decomposition of APB's in Calcic Plagioclase. *Phys. Chem. Miner.* **1980**, *6*, 169–186. [[CrossRef](#)]
36. Hashimoto, H.; Nissen, H.-U.; Ono, A.; Kumao, A.; Endoh, H.; Woensdregt, C.F. High-resolution electron microscopy of labradorite feldspar. In *Electron Microscopy in Mineralogy*; Springer: Berlin/Heidelberg, Germany, 1976; pp. 332–344. ISBN 3-642-66198-X.
37. Lorimer, G.W.; Cliff, G. Analytical Electron Microscopy of Minerals. In *Electron Microscopy in Mineralogy*; Wenk, H.-R., Ed.; Springer: Berlin/Heidelberg, Germany, 1976; pp. 506–519. ISBN 978-3-642-66196-9.
38. Heck, P.R.; Stadermann, F.J.; Isheim, D.; Auciello, O.; Daulton, T.L.; Davis, A.M.; Elam, J.W.; Floss, C.; Hiller, J.; Larson, D.J.; et al. Atom-Probe Analyses of Nanodiamonds from Allende. *Meteorit. Planet. Sci.* **2014**, *49*, 453–467. [[CrossRef](#)]
39. Valley, J.W.; Cavosie, A.J.; Ushikubo, T.; Reinhard, D.A.; Lawrence, D.F.; Larson, D.J.; Clifton, P.H.; Kelly, T.F.; Wilde, S.A.; Moser, D.E.; et al. Hadean Age for a Post-Magma-Ocean Zircon Confirmed by Atom-Probe Tomography. *Nat. Geosci.* **2014**, *7*, 219. [[CrossRef](#)]
40. Peterman, E.M.; Reddy, S.M.; Saxey, D.W.; Snoeyenbos, D.R.; Rickard, W.D.A.; Fougereuse, D.; Kylander-Clark, A.R.C. Nano-geochronology of Discordant Zircon Measured by Atom Probe Microscopy of Pb-Enriched Dislocation Loops. *Sci. Adv.* **2016**, *2*, e1601318. [[CrossRef](#)]

41. Blum, T.B.; Darling, J.R.; Kelly, T.F.; Larson, D.J.; Moser, D.E.; Perez-Huerta, A.; Prosa, T.J.; Reddy, S.M.; Reinhard, D.A.; Saxey, D.W.; et al. Best Practices for Reporting Atom Probe Analysis of Geological Materials. In *Microstructural Geochronology*; American Geophysical Union (AGU): Washington, DC, USA, 2017; pp. 369–373. ISBN 978-1-119-22725-0.
42. La Fontaine, A.; Piazzolo, S.; Trimby, P.; Yang, L.; Cairney, J.M. Laser-Assisted Atom Probe Tomography of Deformed Minerals: A Zircon Case Study. *Microsc. Microanal.* **2017**, *23*, 404–413. [[CrossRef](#)]
43. White, L.F.; Kizovski, T.V.; Tait, K.T.; Langelier, B.; Gordon, L.M.; Harlov, D.; Norberg, N. Nanoscale Chemical Characterisation of Phase Separation, Solid State Transformation, and Recrystallization in Feldspar and Maskelynite Using Atom Probe Tomography. *Contrib. Mineral. Petrol.* **2018**, *173*, 87. [[CrossRef](#)]
44. Valley, J.W.; Reinhard, D.A.; Cavosie, A.J.; Ushikubo, T.; Lawrence, D.F.; Larson, D.J.; Kelly, T.F.; Snoeyenbos, D.R.; Strickland, A. Nano- and Micro-Geochronology in Hadean and Archean Zircons by Atom-Probe Tomography and SIMS: New Tools for Old Minerals. *Am. Mineral.* **2015**, *100*, 1355–1377. [[CrossRef](#)]
45. Dyck, O.; Leonard, D.N.; Edge, L.F.; Jackson, C.A.; Pritchett, E.J.; Deelman, P.W.; Poplawsky, J.D. Accurate Quantification of Si/SiGe Interface Profiles via Atom Probe Tomography. *Adv. Mater. Interfaces* **2017**, *4*, 1700622. [[CrossRef](#)]
46. Devaraj, A.; Colby, R.; Hess, W.P.; Perea, D.E.; Thevuthasan, S. Role of Photoexcitation and Field Ionization in the Measurement of Accurate Oxide Stoichiometry by Laser-Assisted Atom Probe Tomography. *J. Phys. Chem. Lett.* **2013**, *4*, 993–998. [[CrossRef](#)]
47. La Fontaine, A.; Gault, B.; Breen, A.; Stephenson, L.; Ceguerra, A.V.; Yang, L.; Dinh Nguyen, T.; Zhang, J.; Young, D.J.; Cairney, J.M. Interpreting Atom Probe Data from Chromium Oxide Scales. *Ultramicroscopy* **2015**, *159*, 354–359. [[CrossRef](#)]
48. Gault, B.; Saxey, D.W.; Ashton, M.W.; Sinnott, S.B.; Chiamonti, A.N.; Moody, M.P.; Schreiber, D.K. Behavior of Molecules and Molecular Ions near a Field Emitter. *New J. Phys.* **2016**, *18*, 033031. [[CrossRef](#)]
49. Petrishcheva, E.; Tiede, L.; Schweinar, K.; Habler, G.; Li, C.; Gault, B.; Abart, R. Spinodal Decomposition in Alkali Feldspar Studied by Atom Probe Tomography. *Phys. Chem. Miner.* **2020**, *47*, 30. [[CrossRef](#)] [[PubMed](#)]
50. Yund, R.A. Interdiffusion of NaSi—CaAl in Peristerite. *Phys. Chem. Miner.* **1986**, *13*, 11–16. [[CrossRef](#)]
51. Liu, M.; Yund, R.A. NaSi—CaAl Interdiffusion in Plagioclase. *Am. Mineral.* **1992**, *77*, 275–283.
52. Atkinson, A.J.; Carpenter, M.A.; Salje, E.K.H. Hard Mode Infrared Spectroscopy of Plagioclase Feldspars. *Eur. J. Mineral.* **1999**, *11*, 7–21. [[CrossRef](#)]
53. Carpenter, M.A. Equilibrium Thermodynamics of Al/Si Ordering in Anorthite. *Phys. Chem. Miner.* **1992**, *19*, 1–24. [[CrossRef](#)]
54. Carpenter, M.A.; Ferry, J.M. Constraints on the Thermodynamic Mixing Properties of Plagioclase Feldspars. *Contrib. Mineral. Petrol.* **1984**, *87*, 138–148. [[CrossRef](#)]
55. Carpenter, M.A. Mechanisms and Kinetics of Al-Si Ordering in Anorthite: I. Incommensurate Structure and Domain Coarsening. *Am. Mineral.* **1991**, *76*, 1110–1119.
56. Phillips, E.R.; Chenhall, B.E.; Stone, I.J.; Pemberton, J.W. An Intergrowth of Calcific Labradorite in a Plagioclase-Quartz-Biotite Gneiss from Broken Hill, New South Wales. *Mineral. Mag.* **1977**, *41*, 469–471. [[CrossRef](#)]
57. Vinograd, V.L.; Putnis, A.; Kroll, H. Structural Discontinuities in Plagioclase and Constraints on Mixing Properties of the Low Series: A Computational Study. *Mineral. Mag.* **2001**, *65*, 1–31. [[CrossRef](#)]
58. McLaren, A.C.; Marshall, D.B. Transmission Electron Microscope Study of the Domain Structures Associated with the *b*-, *c*-, *d*-, *e*- and *f*-Reflections in Plagioclase Feldspars. *Contrib. Mineral. Petrol.* **1974**, *44*, 237–249. [[CrossRef](#)]
59. Wenk, H.-R.; Joswig, W.; Tagai, T.; Korekawa, M.; Smith, B.K. Average Structure of An 62-66 Labradorite. *Am. Mineral.* **1980**, *65*, 81–95.
60. Parsons, I.; Brown, W.L. Mechanisms and Kinetics of Exsolution—Structural Control of Diffusion and Phase Behavior in Alkali Feldspars. In *Diffusion, Atomic Ordering, and Mass Transport*; Advances in Physical Geochemistry; Springer: New York, NY, USA, 1991; pp. 304–344.
61. Carpenter, M.A. Experimental Delineation of the “*e*” \rightleftharpoons $\bar{I}\bar{I}$ and “*e*” \rightleftharpoons $\bar{C}\bar{I}$ Transformations in Intermediate Plagioclase Feldspars. *Phys. Chem. Miner.* **1986**, *13*, 119–139. [[CrossRef](#)]
62. Carpenter, M.A.; McConnell, J.D.C.; Navrotsky, A. Enthalpies of Ordering in the Plagioclase Feldspar Solid Solution. *Geochim. Cosmochim. Acta* **1985**, *49*, 947–966. [[CrossRef](#)]
63. Carpenter, M.A.; McConnell, J.D.C. Experimental Delineation of the $\bar{C}\bar{I}\rightleftharpoons\bar{I}\bar{I}$ Transformation in Intermediate Plagioclase Feldspars. *Am. Mineral.* **1984**, *69*, 112–121.
64. Parsons, I.; Fitz Gerald, J.D.; Lee, M.R. Routine Characterization and Interpretation of Complex Alkali Feldspar Intergrowths. *Am. Mineral.* **2015**, *100*, 1277–1303. [[CrossRef](#)]
65. Hoshi, T.; Tagai, T. TEM Investigation of Potassium-Calcium Feldspar Inclusions in Bøggild Plagioclase. *Am. Mineral.* **1997**, *82*, 1073–1078. [[CrossRef](#)]
66. Wenk, H.-R. An albite-anorthite assemblage in low-grade amphibolite facies rocks. *Am. Mineral.* **1979**, *64*, 1294–1299.